UNIVERSITY OF CALGARY

Two Approaches to Improving the Utility of Electrical Conductivity in Time Varying Porous Media: Numerical Modeling and Preliminary Field Inversions

by

Archa Rowan B. Cockett

A THESIS
SUBMITTED TO THE FACULTY OF UNDERGRADUATE STUDIES
IN PARTIAL FULFILMENT OF THE REQUIREMENTS FOR THE
DEGREE OF HONORS IN APPLIED AND ENVIRONMENTAL GEOLOGY

DEPARTMENT OF SCIENCE, GEOSCIENCE
CALGARY, ALBERTA
APRIL, 2010

UNIVERSITY OF CALGARY
FACULTY OF GRADUATE STUDIES

The undersigned certify that they have read, and recommend to the Faculty of Graduate Studies for acceptance, a thesis entitled " Two Approaches to Improving the Utility of Electrical Conductivity in Time Varying Porous Media: Numerical Modeling and Preliminary Field Inversions" submitted by Archa Rowan B. Cockett in partial fulfillment of the requirements of the degree of Honors in Applied and Environmental Geology.

_____

Supervisor, Dr. Adam Pidlisecky, Geoscience

_____

Dr. Larry Bentley, Geoscience

_____

Date

Abstract

Electrical conductivity (EC) is sensitive to hydrologic parameters such as pore fluid EC, soil porosity, and water saturation. Empirical relations, such as Archie's law, correlate these hydrogeologic parameters and measured EC. However, these laws do not yet provide an adequate method for the analysis of dynamic unconsolidated sediment. A managed aquifer recharge project in California is the motivation for this thesis; four high-quality time-lapse EC probes were installed to monitor infiltration beneath an artificial recharge pond. As a way of improving the utility of these EC data I undertook two distinct studies: 1) development of a pore scale numerical rock physics model of unconsolidated sediments, and 2) preliminary inversion analysis of the field data.

The pore-scale numerical model was created to investigate time-lapse electrical response of unconsolidated sediment through the use of two porosity reduction algorithms: 1) addition of fine sediment; and 2) biological clogging. This numerical model explores the effects of hydraulic parameters on the measured bulk EC of a fresh-water saturated, unconsolidated, idealized sediment pack. The results and implications of this numerical model were threefold: 1) a series of ranges, values, and relationships that are applicable to the artificial recharge pond; 2) conceptualization of the relative effects of different hydrogeologic parameters of bulk EC; and 3) a series of code that can be adapted to various pore-scale modeling problems.

The preliminary inversion analysis examined several methods of including *a priori* information in the inversion program. This initial inversion process illustrates several of the problems with the current methods available for the analysis of time-lapse EC data. A combination of the information gleaned from the pore-scale numerical model with the high-quality EC data will produce greater interpretive power in future work.

Acknowledgements

Funding for this research was from: the Program for Undergrad Research Experience (PURE) and the start-up grant of Dr. Adam Pidlisecky. Funding for the acquisition of the field conductivity data was provided by Schlumberger Water Services through a grant to Rosemary Knight and the GEM Center, at Stanford University. In addition I would like to thank: Dr. Larry Bentley for his constructive criticism; and Dr. Robin Cockett for his thoughts on algorithm development. We also want to thank Brian Lockwood and Mary Bannister, of the Pajarro Valley Water Management Agency, for providing access to the Watsonville infiltration pond that was the impetus for this work.

Table of Contents

List of Tables

List of Figures and Illustrations

Chapter One: Introduction

1.1 Introduction to Electrical Conductivity

Electrical conductivity (EC) is a physical property that quantifies the ease with which electric current can flow in a material. In sediment, the majority of electrical flow occurs in the fluid phase between connected pores. Thus, EC is sensitive to the quantity of pore water, the quality of the pore water (with respect to total dissolved solids), and the connectivity of pores (Archie, 1942). Given these relations, EC measurements are of particular interest to some scientists working in the near-surface; the near-surface is approximately the top 100m of the Earth's surface. EC measurements have many applications including: delineation of electrically conductive contamination plumes (Atekwana *et al.*, 2000; Benson *et al.*, 1997; Urish, 1983); mineral exploration (Harinarayana, 1999) ground water table monitoring and interpretation (French & Binley 2004); estimations of water saturation in oil reservoirs as well as in the near surface (Garambois *et al.*, 2002; Archie, 1942); and investigations of temporal and spatial locations of biodegredation of organic contaminants (Werkema *et al.*, 2003). The wide uses of EC are in part due to the ease of data collection, the use of automated equipment, and the ability to collect temporally and spatially exhaustive field measurements, relative to traditional point sampling methods. One major challenge, however, with using conductivity data is understanding exactly how these measurements depend on the properties of the subsurface. While it is qualitatively clear that pore water quality, connectivity, and quantity effect EC, exploring the quantitative relationships between these parameters and measured conductivity is of paramount importance to increasing the utility of conductivity measurements for inferring hydrogeologic parameters. Examining how the electrical response of sediment changes over time is another important aspect to consider. Creating time-varying rock physics relationships that link EC data to pore water quality, connectivity, and quantity, is necessary to generate a deeper hydrogeologic understanding.

1.2 Governing Equations

EC experiments are implemented by applying a known electrical current to the subsurface and measuring the resulting voltages. The voltage response is governed by Poisson's equation, with appropriate boundary conditions applied (Pidlisecky *et al.*, 2007):

$$\nabla \cdot (-\sigma \nabla \phi) = I(\delta(r - r_{s+}) - \delta(r - r_{s-})) \tag{1.1}$$

where σ is the conductivity structure; ϕ is the electrical potential field; and I is the electrical current from a dipole. In a typical measurement there is current applied over positive and negative current sources (r_{s+} and r_{s-} respectively); these locations are included using a Dirac delta function (Pidlisecky *et al.*, 2007). Equation 1.1 is linear, and is solved numerically; thus it is easier to represent this equation in matrix notation (Pidlisecky *et al.*, 2007):

$$\mathbf{(DS(\sigma)G)u = A(\sigma)u = q} \tag{1.2}$$

where **D** and **G** are the divergence and gradient operators in matrix form; **S**(σ) is the conductivity structure as a diagonal matrix containing the conductivity values; **u** contains the electric potentials; and **q** is a vector containing the locations of the positive and negative receiver locations. Rearranging Equation 1.2 to solve for the potential field yields:

$$\mathbf{u = A^{-1}(\sigma)q} \tag{1.3}$$

However, the physically measured data is only a subset of the total potential field and must be found with a projection matrix (**Q**), which is programmed for the specific data set.

$$\mathbf{d = Qu = QA^{-1}(\sigma)q} \tag{1.4}$$

These equations are necessary to model electrical potentials, and will be used in the following chapters. It is noted, that these equations only allow for calculation of measured data given a conductivity structure; often the conductivity structure is of interest when measured data is provided. This non-linear inverse problem will be discussed in Section 1.5; however, simplified expressions of Poisson's equation that assume a homogeneous conductivity structure (σ_h) can provide a direct relationship

between the applied current, measured voltage, and the homogeneous conductivity value of interest. For example, EC measurements of a core sample in a laboratory setting allow for boundary conditions on the electrical flow, thus Poisson's equation simplifies to a simple linear expression.

1.3 Laboratory Measurements

Laboratory measurements of EC allow for accurate and controlled experiments; these data and are often tied to field scale results to aid in hydrogeologic interpretation. In the near-surface, unconsolidated sediment samples are obtained and often need to be repacked in the lab to create representative conditions. An electrical current (*I*) is applied to this core sample and the potential drop (*V)* is measured; using Ohm's law, the total resistance (*R)* of the core sample can be calculated. Due to the simple geometric arrangement of this experiment and the known boundary conditions, Poisson's equation can be simplified. The homogeneous or bulk EC ($\sigma_{b)}$ as well as the inverse of conductivity: bulk resistivity ($\rho_{b)}$, is calculated as followed:

$$\sigma_b = \frac{1}{\rho_b} = \frac{l}{RA} = \frac{Il}{VA} \tag{1.5}$$

EC is dependent on both the cross-sectional area of current flow (*A*) and the length of the sample (*l)*. In a lab experiment both of these geometries are well defined (Figure 1.1a); thus, the bulk conductivity of the sample can be easily calculated.

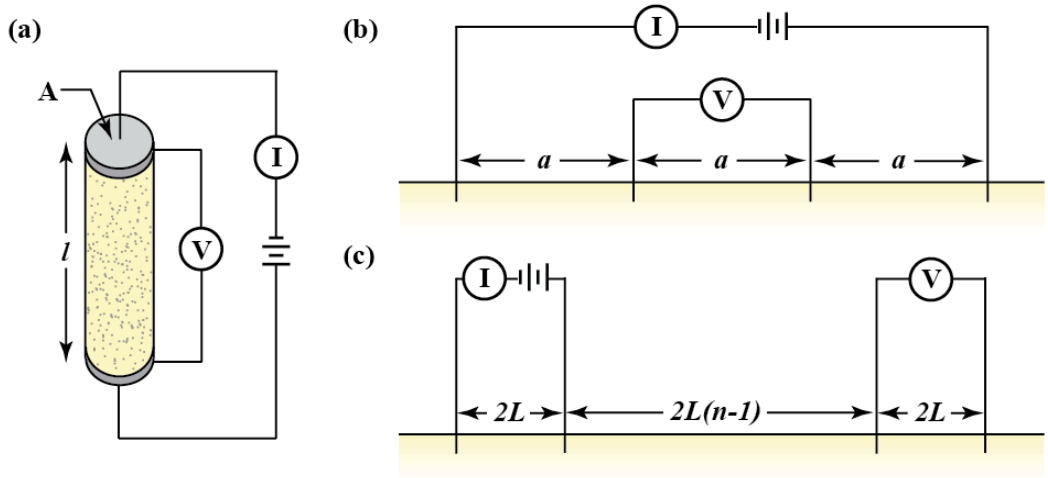

Figure 1-1: Three ways of obtaining EC measurements; (a) lab measurements are generally made over a core sample. Field conductivities can be obtained using various spreads: (b) the Wenner array, and (c) the dipole-dipole array are commonly used.

1.4 Field Measurements

Measuring EC in a field situation poses more complexity and uncertainty in the conductivity structure. In a field experiment electrodes are placed in the ground using stakes or probes for horizontal and vertical acquisition systems respectively. The geometric volume that is sampled by these electrodes depends on the sequence and layout of the acquisition system as well as the conductivity structure of the sediment. Identifying this geometric factor allows for conversion of conductance measurements into conductivity values; or similarly, resistance measurements into resistivity values. In the lab experiment illustrated in Figure 1.1a, the geometric factor is the length of the core sample over the cross sectional area; this geometric factor is then multiplied by the calculated conductance (Eq. 1.5). In the field setting, to find a homogeneous conductivity value a simplified expression of Poisson's equation is used. Specific types of arrays are used to find homogeneous EC values including the Wenner array and the dipole-dipole array.

The Wenner array, seen in Figure 1.1b, requires that electrodes have an equal spacing, a, which can be widened to increase the depth of measurement or the a-spacing can be shortened to reduce the volume averaging. When using surface electrodes, the homogeneous conductivity for the Wenner array reduces Poisson's equation to (Telford *et al.*, 1990):

$$\sigma_h = \frac{I}{2\pi aV} \tag{1.6}$$

The dipole-dipole array, seen in Figure 1.1c, requires that the potential and the current electrode pairs are at the same tight spacing ($2L$) and that the dipoles are widely separated ($2L \cdot (n-1)$, where n is an integer). Under these conditions Poisson's equation reduces to (Telford *et al.*, 1990):

$$\sigma_h = \frac{I}{2\pi n^3 LV} \tag{1.7}$$

In both the field and laboratory acquisition systems, it is possible to reverse the current, as well as interchange the locations of the current and potential electrodes to increase the number of measurements taken; these reverse measurements should be identical.

These simple arrays were developed to make the calculation of homogeneous conductivity easy to obtain, because they use closed formed solutions of Poisson's equation. It should be noted, however, that the homogeneous conductivity is the conductivity of the theoretical homogeneous half space that would yield the measured voltage drop with the applied current. As a bulk average this measurement fails to capture the variability and heterogeneity of the sediments conductivity structure. In modern EC surveys, the arrays use a multitude of overlapping measurements that can be combined to gain a higher resolution model of the subsurface. The study of combining data that have some parts of single measurements in common is called inverse theory.

1.5 Inversion of Field Data

Inversion of EC data results in non-linear optimization problem. This is a challenging problem to solve because it is often underdetermined, meaning that the number of observational data is much less than the number of model parameters. For the inversion of field data RESINVM3D was used to solve the inverse problem numerically (Pidlisecky *et al.*, 2007). This program uses a two-part objective function:

$$\Phi(\mathbf{m}) = \frac{1}{2}\left\|\mathbf{QA^{-1}(m)q - d_{obs}}\right\|^2 + \frac{\beta}{2}\left\|\mathbf{W(m - m_{ref})}\right\|^2 \qquad (1.8)$$

The first term minimizes the data misfit, where $\mathbf{QA^{-1}(m)q}$ is the data produced by the forward modeling code given a conductivity model (σ) (Eq. 1.4); and $\mathbf{d_{obs}}$ is the observed data in vector form. The second term accounts for the under determination of the problem and contains *a priori* knowledge about the model distribution; β is a regularization parameter that provides a balance between model regularization and data misfit; **W** is a matrix that controls smoothing; **m** is the model at any given iteration; and $\mathbf{m_{ref}}$ is the reference or starting model. RESINVM3D allows for input of *a priori* knowledge in the form of amount, and direction of smoothness allowed by the inversion, as well as deviation from the starting model. The result of this inversion program is an estimate of EC at all spatial and temporal locations.

1.6 Rock Physics

EC measurements are in themselves very uninformative about hydrogeologic parameters. Rock physics, or petrophysics, is the study of linking geophysical parameters (in this case: EC) to parameters of interest, such as porosity or pore-water saturation. The most widely used empirical relations between porosity and EC in clean sedimentary rocks is Archie's law (Archie 1942):

$$\frac{\sigma_b}{\sigma_f} = \phi^m S_w^n = \frac{1}{F} \tag{1.9}$$

The formation factor (F), which is relatively constant for a given formation, is composed of bulk EC (σ_b) and fluid conductivity (σ_f). The ratio of bulk to fluid EC, Archie's formation factor, is related to the porosity (ϕ) and fluid saturation (S_w). The saturation exponent (n), is an empirical constant that is usually assumed to be approximately two (Archie 1942). The saturation exponent, however, depends on rock type, saturation history, and is difficult to constrain (Rein *et al.*, 2004). In saturated porous media (S_w = 1), Archie's law reduces to dependence only on porosity raised to the exponent m, commonly referred to as the cementation exponent. The cementation exponent increases with cementation, ranging from 1.3 for unconsolidated sediment to 2.5 for consolidated materials (Archie 1942, Sen *et al.*, 1981, Glover 2009). The application of Archie's law in field experiments is often underdetermined: fluid conductivity and porosity are often unknown and water saturation is difficult to determine. Laboratory experiments can be completed to find site-specific parameters, petrophysical relations, or Archie exponents (m and n); simplifying assumptions about spatial and temporal continuity are also commonly applied. However, if laboratory experiments are not completed, Archie exponents, and occasionally porosity values, are assigned using literature values and ranges; these assumptions can greatly reduce the quality of the interpretation.

1.7 Motivation – The Pond

Given that: a) EC measurements allow inferences about the conductivity structure of the subsurface, and b) rock physics can link this structure to hydrogeophysical parameters; it is possible to use these electrical techniques to monitor hydrogeologic

processes. In particular, this thesis considers the monitoring of infiltration for subsurface water storage using EC measurements. Managed Aquifer Recharge has received attention over the past ten years as a way to manage groundwater resources. An artificial recharge pond: Harkins recharge pond, or simply "the pond", has been designed in Pajaro Valley, California for the subsurface storage of water. The Pajaro Valley is an area of intensive agriculture that derives the majority of its irrigation water from groundwater resources. This valley faces problems from over allocation of groundwater and saltwater aquifer intrusions. Pajaro Valley receives the majority of its precipitation in the winter months with the summer months being very dry; additionally, only a small portion of the winter precipitation recharges the costal aquifers naturally. The Pajaro Valley Water Management Agency has developed an aquifer recharge system for growers near Harkins Slough. Winter runoff is filtered and pumped out of Harkins Slough into the pond and is allowed to percolate into a sand aquifer; this percolated water is then recovered in the summer for irrigation purposes.

The hydrogeology beneath the recharge pond has been studied by Haines *et al.* (2009) using cone penetrometer and seismic reflection data as well as borehole drillers' logs. Haines *et al.* (2009) found that there is a thick and continuous clay layer ~35-50m below the recharge pond (Figure 1.2). Above this clay there is ~3-5m of sand and gravel layers. The top ~20-30m below the pond is clean sand with occasional and assumed discontinuous clay layers (<2m thick). Using combined seismic and cone penetrometer data, Haines *et al.*, (2009) found that there may be a continuous clay layer within the upper sand unit. The hydrogeologic interpretation of the site is a ~25-40m thick perched unconfined highly permeable aquifer underlain by a clay aquitard which is ~1-5m thick. In the perched unconfined aquifer there are possible clay lenses that, although assumed to be discontinuous, may be connected providing a barrier to vertical flow. The recharged water beneath the pond is conceptualized to be stored in this perched unconfined aquifer and recovered at the base of the unit in the more permeable layer (Haines *et al.*, 2009).

There are two key issues at Harkins Slough: 1) only 40% of the total allotted water is able to be infiltrated into the subsurface, and 2) only 15% of the infiltrated water is recovered by wells. Research is ongoing for the recovery of the water, and may be due

to the possible continuous clay layer described by Haines *et al.*, (2009) diverting or retaining water outside the recovery wells' capture zones. However, before the water can be recovered it must first infiltrate efficiently and effectively so that more water is stored in the subsurface: i.e. issue 1. Over the winter, recharge rates start high; however, as the

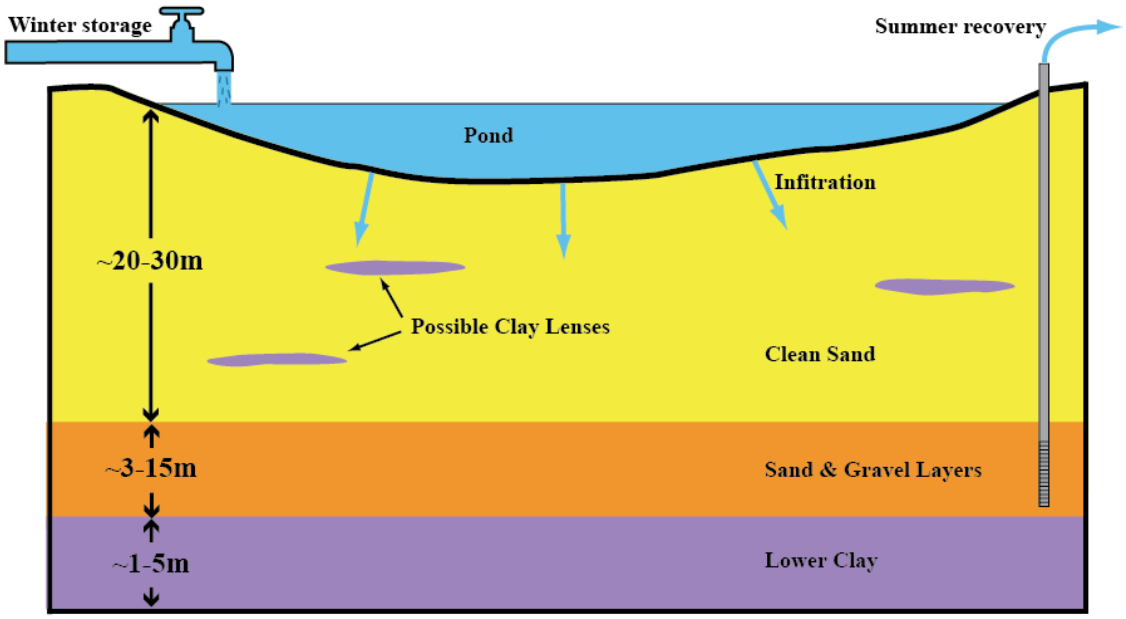

Figure 1-2: Conceptual model of the hydrogeology beneath the Harkins recharge pond in Pajaro Valley, California. Adapted from Haines *et al.*, (2009).

infiltration continues the pond infiltration slows dramatically. Two alternative mechanisms are hypothesized this reduction in infiltration. The first mechanism is clogging through sedimentation, shown in Figure 1.3a. Although the water that is collected in the pond is first pumped through sand-filters, some clay-sized particles are retained and suspended in the water column. Over the length of the infiltration, these fine particles settle out and create a less permeable layer over the pond bottom. This process is combated via tilling of the pond bottom before the infiltration begins, when the pond is dry. The second mechanism is biological clogging, shown in Figure 1.3b. The water used for recharge is runoff from a highly agricultural area and has elevated nitrate concentrations (Racz *et al.*, 2009). These nutrients are hypothesized to elevate biological growth in the water column as well as the top few meters of the unconfined aquifer. This biological growth can lead to changes in porosity, surface area, pore geometry, tortuosity, and Archie's formation factor (Atekwana *et al.*, 2006). Creation of biofilms may be

another reason for reduced infiltration. These processes reduce infiltration in the late winter and spring, but could also pose problems for long-term maintenance of this recharge pond. To monitor the infiltration process, four EC probes were installed in the bottom of the pond. These probes generate high quality time-lapse conductivity data, and show promise for identifying and solving the key issues associated with the infiltration process at Harkins recharge pond. Two objectives must first be addressed: 1) establishment of robust rock physics relationships at the pond; and 2) inversion of field data to find conductivity structures of the subsurface, which can then be analyzed.

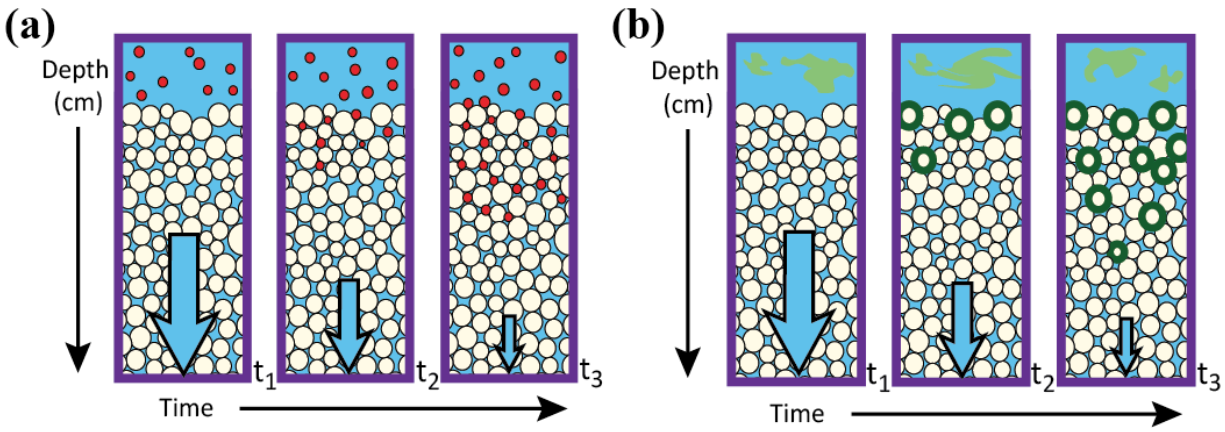

Figure 1-3: Two hypothesized mechanisms to explain the decreased infiltration rates in Harkins Slough at late times: (a) addition of fines to the matrix and (b) biological growth causeing clogging.

1.8 Summary of the Following Chapters

The following two chapters will address: rock physics relationships of unconsolidated sediment and the inversion of field EC data. Chapter 2 focuses on the pore scale processes that control measured EC, with a focus on time-varying porous media. A pore-scale numerical model was created that calculates reductions in porosity through two mechanisms: clogging by fine-grained sediment and clogging by biological growth (Figure 1.3). The forward modeling code in RESINVM3D was employed to simulate the electrical response for a variety of these modeled idealized unconsolidated sediment packs. Additionally, programs were created that calculate modeled sediment parameters, including porosity, surface area, and tortuosity. Factors controlling electrical response were analyzed and rock physics relations were developed to conceptualize differences between the clogging mechanisms. Chapter 3 focuses on inverting field data

from the EC probes in Harkins recharge pond. A methodology is created for inverting the field data, and it is shown that the formation factor is spatially and temporally variable. This variability is dealt with using the knowledge and rock physics gleaned from the numerical model described in Chapter 2. A summary of the thesis is provided in Chapter 4 that highlights future work and possible directions using this numerical model and field data.

Chapter Two: Numerical Modeling

2.1 State of Numerical Rock Physics

Archie's law was specifically developed for analyzing electrical resistivity logs of clean sedimentary rock saturated with brine (Archie, 1942). However, it has since been used for the investigation of near-surface unconsolidated sediments with fresh water as a saturating fluid (Jayawickreme *et al.*, 2008, Ganerød *et al.*, 2006); there have also been Archie type analysis completed on sediments containing clays, despite the fact that it was not developed for this purpose (Worthington 1993). Archie's formation factor, which is the ratio of bulk conductivity to fluid conductivity, is loosely defined as a constant for any given porous media; however, this formation factor has been seen to vary significantly over time in unconsolidated sediment (Singha & Gorelick, 2006). Formation factor variability could be due to unaccounted changes in porosity or saturation; it is also possible that Archie's law is performing a poor job of describing dynamic sediment (Singha *et al.*, 2008). In unconsolidated sediment it is intrinsically difficult to conduct laboratory experiments that precisely replicate in-situ conditions. Excavation and transport of unconsolidated samples from field sites disturbs the sample and can lead to changes in porosity, isotropy, and packing, as well as other sample characteristics (Lovell *et al.*, 1998). Laboratory sample analysis are also not always performed; this lack of laboratory constraint often leads to the assumption of m=2, which limits the utility of Archie's law and results are often discounted or discredited by other more reliable techniques (Sénéchal *et al.*, 2005, Garambois *et al.*, 2002).

In near-surface geophysics Archie's law is currently used to obtain porosity, water saturation, pore water conductivity, and contaminant concentrations and mass (Deiana *et al.*, 2008, Worthington 1993). However, to derive robust and accurate values from EC data intensive calibration techniques are required (Jayawickreme *et al.*, 2008). Temporal variation, in terms of percent change, can be used to obtain hydrogeologic properties using Archie parameters that have not been calibrated (Sénéchal *et al.*, 2005). The relation between effective diffusivity, tortuosity, and Archie's cementation exponent is the focus of ongoing research in contaminant processes (Hirono *et al.*, 2007); however, using empirical relations to find theoretical parameters is difficult. For instance, although

the cementation exponent is theorized to be a function of grain and pore geometry, it is used in the literature mainly as a fitting parameter (Glover, 2009); and thus, little information can be gleaned from the cementation exponent. Archie's law is not yet a stand-alone technique for analysis of dynamic near-surface parameters; a multi-proxy approach for corroboration of results from sources such as ground penetrating radar and laboratory soil analysis, provides the most reliable values (Deiana *et al.*, 2008, Sénéchal *et al.*, 2005). A lack of reliability in the results produced by Archie-type methods demonstrates the need for a greater theoretical understanding of the factors that control EC.

Using high-resolution time-lapse electrical data, it is becoming especially apparent that this empirical relation is not up to the task of describing the nuances of dynamic systems. To understand the more complicated theoretical aspects controlling the electrical response significant research, numerical modeling, and continued lab and field experiments are necessary. It should be noted that although Archie's law is a simplified empirical relation, it is widely used, useful in field assessment, and can be used to show temporal changes effectively if Archie exponents are held constant at arbitrary values.

A numerical model was constructed to better understand the factors that control measured EC in porous media. This model simulates the EC response for a variety of idealized sediment packs. Algorithms were developed to perturb these idealized packs to represent temporal changes in porosity and pore-space configuration through two mechanisms: addition of fines to the matrix (Figure 1.3a) and biological growth on grain surfaces (Figure 1.3b).

2.2 The Numerical Model

A numerical model was created that enables well controlled experiments, in which each hydrogeologic parameter of interest can be either defined or determined. This allows for the study of the relationships between porosity, electrical tortuosity, specific surface area, and bulk EC in idealized saturated unconsolidated sediment. The developed numerical model simulates laboratory measurements of EC on small, idealized, unconsolidated sediment packs. Modeling experiments rather than laboratory

experiments have the advantage of investigating parameters that otherwise could not be controlled.

2.2.1 Measuring Bulk Electrical Conductivity

A numerical model was created that simulates DC-conductivity measurements on unconsolidated sediment at the pore scale. The model simulates a variety of saturated porous media through discretization of sphere packing arrangements on a three-dimensional grid. To simulate bulk EC, current was injected over the entire end of an approximately 1.0 by 1.0 by 1.0 cm packing model; this end plate is seen in yellow in Figure 2.1. The end plate conductivity was the same as the fluid conductivity, and would be similar to a lab experiment using an electrode plate that is in contact with a sediments saturating fluid. As the dimensions of the model are known it is simple to calculate a bulk conductivity given current and voltage measurements (Eq. 1.5). The current over the end plates was defined and the resulting potential field was found using a three-dimensional finite-volume forward modeling code that solved Poisson's equation (Pidlisecky *et al.*, 2007); see Section 1.2. Each ~1.0 cm^3 sample was discretized on a three-dimensional grid containing up to 16.5 million voxels, where each cubic voxel has dimensions less than 62.5 μm on each side. A portion of a discretized model is seen in Figure 2.1 with voxel boundaries seen in grey. For models containing 16.5 million voxels it took approximately 36 hrs to run a forward model using four cores of a 3Ghz Xeon processor, equipped with 64Gb of ram. The bulk EC of each sample was calculated by averaging over the entire area of the two end plates. The ratio between grain and fluid EC was made large enough to eliminate effects of grain conduction.

2.2.2 Idealized Sediment Pack

Six random sphere packs from three different uniform grain size distributions were modeled along with two ordered packs: a simple cubic pack ($\phi = 0.4764$) and a hexagonal close pack ($\phi = 0.2584$). The six random sphere packs contained two realizations from each of the following uniform grain size distributions: random packs had grain diameters of 0.80 – 1.20 mm; 1.00 – 1.00 mm; and 1.00 – 1.50 mm. The disordered packs were created using the packing model of Jodrey and Tory's (1979). This

model simulates sedimentation through the settling of a dilute suspension. Their algorithm results in a grain pack with some anisotropy, as the pack is less dense in the settling direction. These directional density differences translate into slight changes in EC depending on the primary sampling direction of the electrodes; unless otherwise stated, the primary sampling direction was defined to be perpendicular to the settling direction. The packing model does not allow for changes in porosity and creates models with porosities between 0.39 and 0.43. By iteratively decreasing the dimensions of the voxels in a model and observing the response of EC, the optimum model discretization was found. This optimum was a balance between maximizing the voxel size and minimizing numerical anomalies due to artificial grain surface roughness; the optimum model discretization was found to be dependant on the grain size distribution.

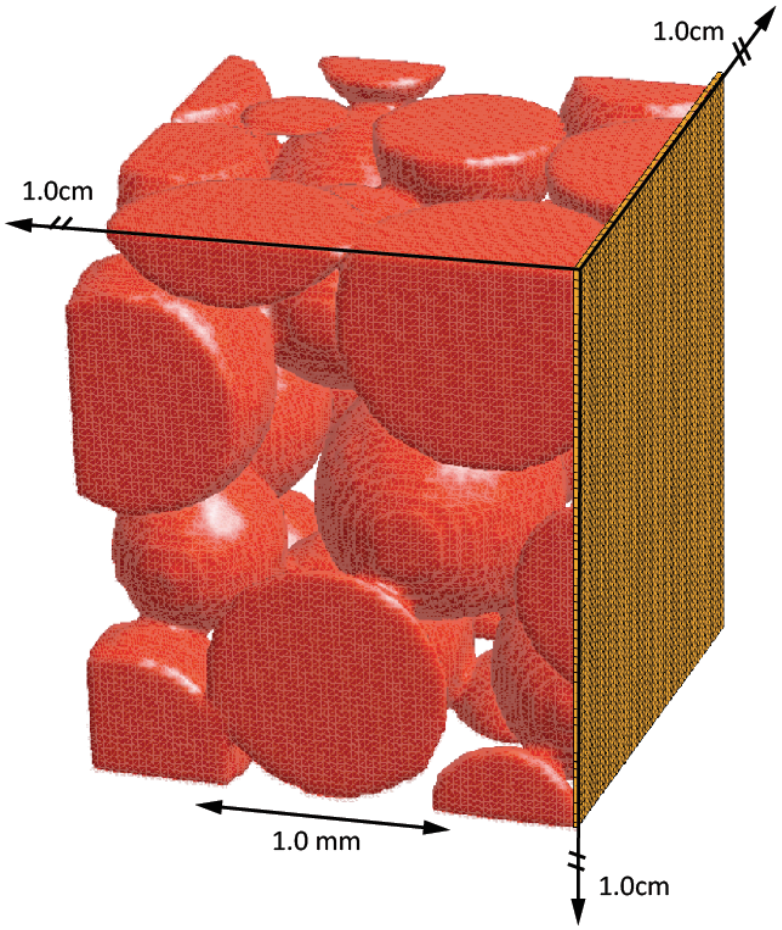

Figure 2-1: Portion of a disordered pack showing grains (red spheres) that have been discretized; voxel boundaries are superimposed on the grains and are shown in grey. The endplate is shown in yellow with voxel boundaries shown in black.

2.3 Pack Properties

Electrical conductivity is dependent on the interaction between many hydrogeologic parameters. The porosity, specific surface area, and electrical tortuosity of each model was calculated to see each specific relationship with bulk EC.

2.3.1 Porosity

Porosity is an intimate player in EC response as recognized by Archie (1942) in his empirical equation Archie's law (Eq. 1.9). Porosity was determined by first finding the volume of the void space (V_V) that is represented by empty voxels in the model. The volume void space is then divided by the total volume of the sample (V_T), which is represented by the total number of voxels.

$$\phi = \frac{V_V}{V_T} \tag{2.1}$$

Porosity of the random packs ranges from 0.39 to 0.43. The porosity of the simple cubic pack is 0.4764 and the hexagonal close pack has a porosity of 0.2584. These two ordered packs were viewed as unconsolidated sediment end members in subsequent experiments.

2.3.2 Specific Surface Area

Specific surface area of a sample is related to the grain size range and distribution, degree of cementation, and grain angularity. Specific surface area is an intuitive parameter to estimate, and because it is tied to factors that influence electrical and hydraulic conductivity, it is of interest to hydrogeologists. The specific surface area (S_S) of a sample is the total surface area (S_T) normalized by the total volume of the sample (V_T), as shown in Equation 2.2.

$$S_S = \frac{S_T}{V_T} \tag{2.2}$$

The total surface area of the model was calculated using a hybrid analytical/numerical solution that computes the surface area of each individual grain, and sums the results. For the case of simple grain to grain overlaps (involving only two grains), an analytical solution was used. The surface area of a spherical cap within an overlapping sphere or outside the model space was subtracted from the surface area of the total sphere. The

surface area of a spherical cap (A_{SC}) depends on the radius of the sphere (r) and the height of the spherical cap (h):

$$A_{SC} = 2\pi r h_i \tag{2.3}$$

A diagram of a spherical cap schematically illustrating the simple intersection of two grains overlapping is shown in Figure 2.2a. Complicated geometries were defined as those spheres involving multiple grains overlapping the same surface area on the sphere of interest. This complex geometry is seen in Figure 2.2b; note the overlapping area between the two spherical caps. The surface of these spheres was approximated by a fine triangular Delaunay mesh. The area of the individual triangles in this mesh was summed using Heron's formula to obtain an estimate of surface area; the estimate was within 0.1% of the true surface area value in most cases.

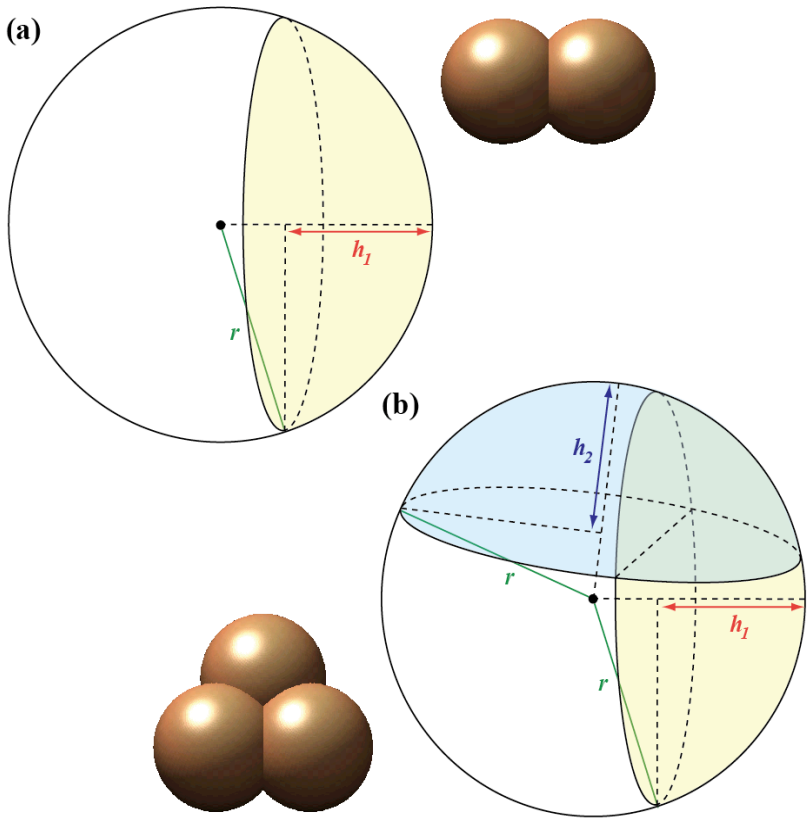

Figure 2-2: Scematic showing surface area of a spherical cap for two general cases: (a) simple grain to grain overlaps and (b) complicated case of multiple overlaps intersecting. Adapted from Weisstein (2010).

2.3.3 Electrical Tortuosity

Tortuosity is a measure of the deviation of a flow path from a straight line. The cementation exponent in Archie's law has been attributed in part to changes in tortuosity (Azar *et al.*, 2008, Boving & Grathwohl 2001). Thus, the investigation of tortuosity is important to the understanding of bulk EC. A clear distinction has evolved in the literature over the past five decades between electrical and hydraulic tortuosity due to the viscosity of fluids causing mixing, and hence a longer flow path when compared to ion movement (Suman & Ruth 1993; Pérez-Rosales 1982; Wyllie & Spangler 1952). Multiple equations have been derived in the literature for electrical tortuosity. The majority of these equations have their roots in the empirical based Archie's law; see Table 2.1 for various statements of tortuosity in the literature that are derived from Archie's law. Interestingly, these equations for electrical tortuosity, which use Archie's formation factor and cementation exponent, are being used to model saturated contaminant transport; which assumes hydraulic tortuosity (Hu & Wang 2003). However, there is interrelation between hydraulic and electrical tortuosity especially in saturated porous media (Wyllie & Spangler 1952).

Table 2.1: Equations found in the literature relating tortuosity to parameters in Archie's law.

Tortuosity Equation	Literature Source
$\tau = \phi^{1-m}$	(Glover 2009, Hu & Wang 2003)
$\tau = \sqrt{F\phi}$	(Herrick & Kennedy 1994)
$\tau = (F\phi^{m})^{x}$	(Azar *et al.*, 2008)
$\tau = F^{2}\phi^{2}$	(Wyllie & Spangler, 1952)
$\tau = F\alpha$	(Suman & Ruth 1993)

x is a correlation constant ($0.5 \leq x \leq 1.5$)
α is aerosity, the porosity in the direction of flow.

In this paper electrical tortuosity will be defined as a geometric average from a distribution of paths a particle travels (L_P) divided by the distance between the ends of each path; i.e. the sample width (L_S) (Eq. 2.4).

$$\tau = \frac{L_P}{L_S} \tag{2.4}$$

The electrical tortuosity of the sphere packs was found by particle tracking through the model. The gradient of the electric potential field was used to determine the flow direction. The original pack was smoothed prior to forward modeling to reduce errors in calculating the gradient at grain-fluid boundaries. In addition, particles were allowed to penetrate up to two voxels into a grain (less than 0.1 mm). If particles penetrated deeper into the grains, the results for the particle's path is discarded as it represents a non-physical (but numerically feasible) situation. In a homogeneously conductive fluid the path length is almost the same for both fluid and electrical flow; this relationship becomes more complicated when there is heterogeneity in the porous media. A series of particle paths are shown in Figure 2.3, with the electrical tortuosity distribution plotted as a histogram of single tortuosity values (Eq. 2.4). The histogram of calculated electrical tortuosity is less positively skewed than a hydraulic tortuosity histogram. The longer flow paths in the hydraulic tortuosity distribution are due to viscosity and flow path elongation in grain eddies; positive skew of tortuosity has been found in other numerical models (Spearing & Matthews 1991). In the literature tortuosity is commonly reported as a single number; to compare results to the literature a single tortuosity value must be used to represent each tortuosity distribution. The calculated electrical tortuosity histograms produced by this numerical model approximate log-normal distributions; thus, all reports of electrical tortuosity values are the geometric means of the logged distribution.

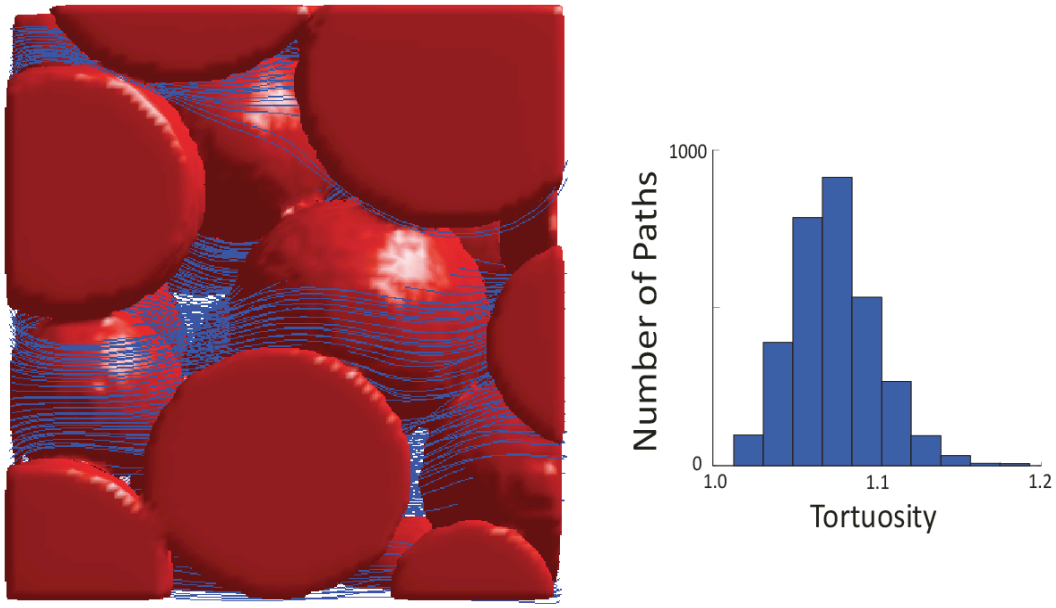

Figure 2-3: Discretized model showing electrical tortuosity paths within the model space and an example of the corresponding histogram showing the length of the paths.

2.4 Experiments

2.4.1 Hydraulic Conductivity

Hydraulic conductivity, and its relation to EC, was explored briefly and by proxy only. Using a series of simple cubic pack, the diameter of the grains was reduced while the porosity was inherently kept constant (Figure 2.4). Using a Kozeny-Carmen (1950) relation (Eq 2.5) it is seen that hydraulic conductivity (*K)* is dependant on grain diameter.

$$K = \frac{\rho g \phi^3 (d_{10})^2}{180 \mu (1-\phi)^2} \tag{2.5}$$

In the case of a single grain diameter constituting the grain size distribution, the tenth percentile (by weight) of grain diameters (d_{10}) is simply input diameter used in the ordered pack. In the case of reducing the diameter of the distribution while holding all other parameters constant (viscosity, μ, density, ρ, porosity, ϕ, and gravity, *g*), it is seen that hydraulic conductivity is only dependant on the diameter of the grain sizes.

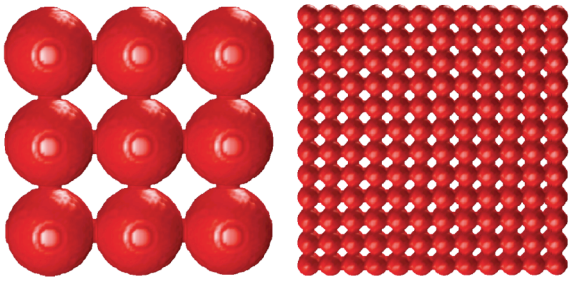

Figure 2-4: A simple cubic pack with variable grain diameters; porosity is constant between models, however, hydraulic conductivity decreases with grain diameter.

2.4.2 Anisotropy

Anisotropy was also modeled in the sphere packs to see this parameters relation to EC. Anisotropy was created in the random packs by increasing the aspect ratio with respect to a single axis. Increase one axis of a sphere, which has an aspect ratio of 1, creates prolate spheroids with two identical axes, and one longer axis (Figure 2.5). The ratio of this single larger axis to the other two equal axes is the aspect ratio. Creation of prolate spheroids introduces anisotropy into the sphere packs, and measurements of EC become dependant on the primary sampling direction (primary electrical flow direction). Bulk EC was measured in three directions: parallel, perpendicular, and normal to the stretching direction. It should be noted that the expansion applied effects the grains and pore space equally, thus does not affect the porosity of the sample. The dimensions of the entire grain pack remained constant, as seen in Figure 2.5, and three different sections at equal spacings along the stretched axis were sampled.

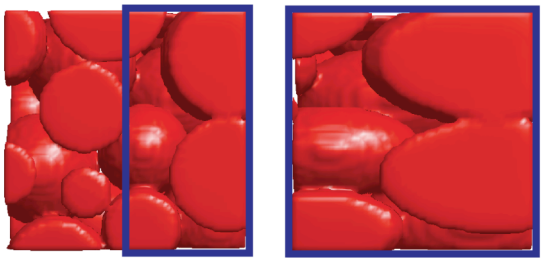

Figure 2-5: Creation of anisotropy from an isotropic disordered sphere pack by applying an aspect ratio expansion of two.

2.4.3 Pack Perturbations

Time-lapse changes in unconsolidated sediment due to addition of fines and biological clogging are of interest to this study. These two mechanisms are attributed

with the reduced infiltration rates in the pond over time. Both of these conceptualized clogging mechanisms require reductions in porosity over time, however, the way in which porosity is reduced is different between the two mechanisms. This numerical model is used to simulate both of these changes, and identify differences between the processes. The sphere packing program generated random grain packs that had a constant porosity of 0.40±0.03. Thus, to explore the effects of porosity and pore-space arrangement on EC two simple algorithms were employed: a grain-addition algorithm (Add) and a grain-growing algorithm (Grow). These two algorithms are depicted schematically in Figure 2.6. The Add algorithm represents the addition of fines to the soil matrix similar to the situation depicted in Figure 1.03a in the pond. The Add algorithm has the greatest effect on pore bodies. The Grow algorithm represents clogging due to a biological film of growth, this process represents the situation depicted in Figure 1.03b in the pond. The Grow algorithm created is similar to schematics on microbe colonization and biofilm creation in Atekwana *et al.*, (2006), where microbe colonies are seen to have the greatest effect on pore throats. A similar grain-growing algorithm has been used in the literature to represent cementation (Roberts & Schwartz 1985).

The Add algorithm works by: (a) creating a list of the largest non-overlapping spheres in each pore space that are centered on a voxel; and (b) spheres are randomly added at locations in the list, until the new pack reaches the specified porosity (Figure 2.4). The spheres that are added also have the condition that their radius must be larger than 200μm. This condition is such that they can be accurately simulated in a reasonable amount of time; in other words multiple voxels must create a single particle to reduce artificial surface roughness, however increasing the discretization of the model space exponentially increases the time to run the model.

The Grow algorithm works by: (a) randomly choosing a grain; and (b) randomly increased that grain's radii by a factor between 1.0 and 1.2; this is continued until a defined porosity is reached (Figure 2.6). The conductivity of the newly added grains in both algorithms was set to the same conductivity as the original grains in the matrix. It should be noted that, this conductivity choice does not model volume conduction of the

biofilm. Additionally, surface conduction was not modeled due to lack of descriptive physics.

These models provide a time-lapse exploration of two simple processes to determine if EC is sensitive to slight changes in pore configuration in two porosity reduction algorithms. These models also allow for investigation of appropriate variability and ranges of Archie's formation factor and cementation exponent as porosity changes. Ranges and variability will provide valuable information for the analysis of uncertainty, methodology, and interpretation of field data.

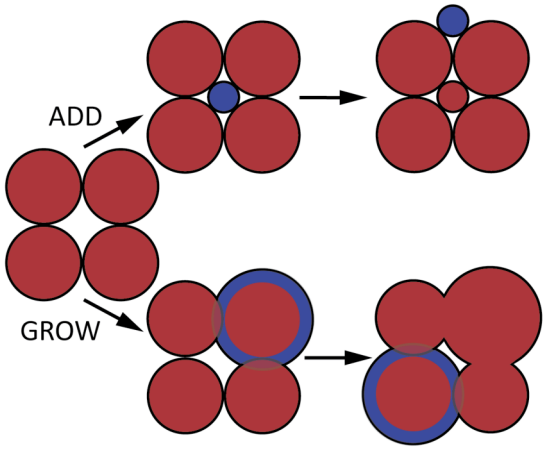

Figure 2-6: The grain-addition algorithm (Add) and the grain-growing algorithm (Grow) applied to a simple cubic pack; both models have the same decrease in porosity.

2.5 Results

2.5.1 Hydraulic Conductivity

Changes in hydraulic conductivity, through reduction in ordered pack's grain size, results in a graph of electrical formation factor that is independent of grain size (Figure 2.7); in this experiment grain size is used as a proxy for hydraulic conductivity (K) (Figure 2.4). The relation between grain size and formation factor for the hexagonal close pack has deviations from a straight line; these are due to very small changes in porosity (<0.01) that occurred when approximating the size of the model space. Decreasing the grain size from 1.5mm to 0.4mm decreases K by an order of magnitude (Carmen 1950). This illustrates that, although influenced by many of the same hydrogeologic parameters, EC and K are not directly related. Stating that EC and K are not directly related does not question the correlation found in the majority of grain packing geometries between EC

and *K*. Both EC and *K* are sensitive to hydrologic parameters such as porosity, saturation, and pore space configuration, however, the specific relation to these hydrologic parameters differs between EC and *K*. Both EC and *K* are governed by Poisson's equation; however, the difference in response is due to the no-slip condition in fluid flow and the difference in dependence in specific surface area between electrical and fluid flow.

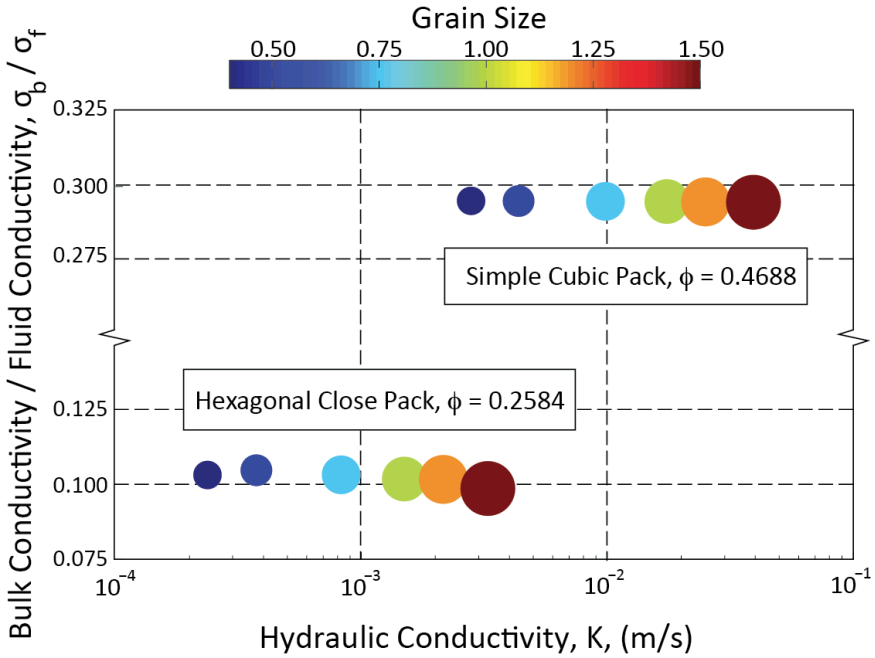

Figure 2-7: Hexagonal close packs and simple cubic packs with variable grain diameters representing a proxy for hydraulic conductivity; EC is not directly dependent on hydraulic conductivity.

2.5.2 Anisotropy

Creation of anisotropy by increasing the aspect ratio in the X direction created an electrical response that was dependent on sampling direction. As seen in Figure 2.8, EC values decreased when sampled perpendicular to the direction stretched (Y and Z), and increased when sampled parallel to the stretching direction (X). The anisotropic packs showed similar results to those found by Sen *et al.* (1981). As the porosity remained relatively constant (within 0.015 of starting porosity), the decrease in EC is likely due to an increase in electrical tortuosity that was found by the model.

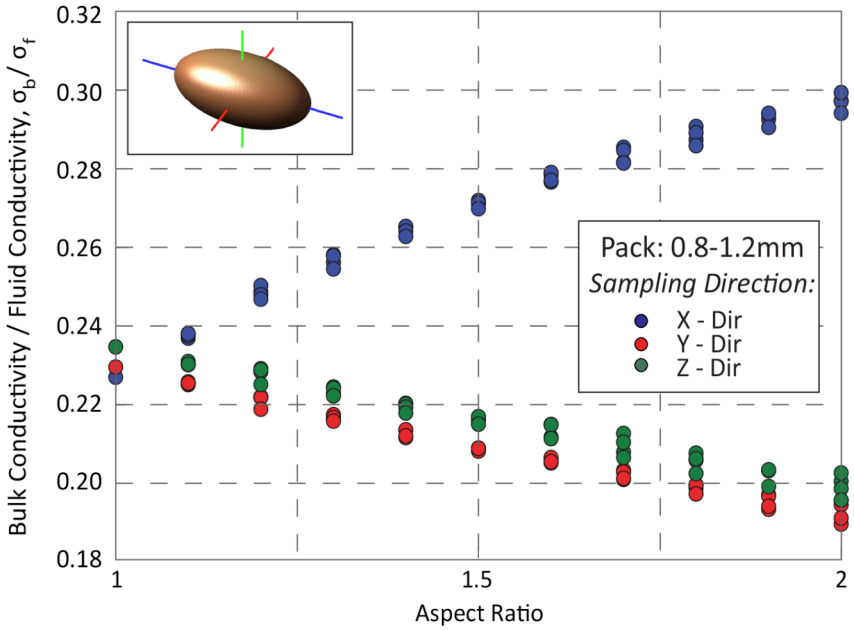

Figure 2-8: EC response to increasing the aspect ratio of the random packs; stretching occurred parallel to the X direction; three samples were taken at equal spacings along the stretched axis to maintain the dimensions of the sample.

2.5.3 Pack Perturbations

The two porosity reduction algorithms, Add and Grow, are shown as filled and outlined symbols, respectively in Figures 2.9 – 2.12. At a porosity of ~0.42 neither of the two algorithms has significantly changed the conductivity of the packs. The calculated cementation exponents of these unperturbed packs were 1.62 ± 0.02, these values are within the range of other EC studies done on unconsolidated sediment (Lovell *et al.*, 1998; Mendelson and Cohen 1982; Sen *et al.*, 1981). The two pack perturbation algorithm results plotted against Archie's cementation exponent are seen in Figure 2.9. As the Grow algorithm decreases the porosity of the packs, the cementation exponent increased linearly with porosity; the norm of residuals from a linear equation is less than 0.03 for all Grow packs. Since the Grow algorithm has also been used as a model for cementation (Roberts and Schwartz 1985), this numerical model confirms the link between cementation and Archie's porosity exponent, *m*. Furthermore, this numerical model suggests that this cementation model acts to increase *m* in a fairly linear fashion.

The Add algorithm responds in a non-linear manner (Figure 2.9). During the first reductions in porosity, Archie's cementation exponent increases. For the packs with an

average grain diameter of 1.0mm (Packs: 0.8-1.2mm & 1.0-1.0mm; see legend), the cementation exponent decreases at a porosity of 0.40 (Figure 2.9); this decrease happens at 0.37 in the packs with a larger average grain diameter of 1.25mm (Packs: 1.0-1.5mm; see legend) (Figure 2.9). This non-linear response may suggest that Archie's law is not the most ideal equation for analyzing these simple packs.

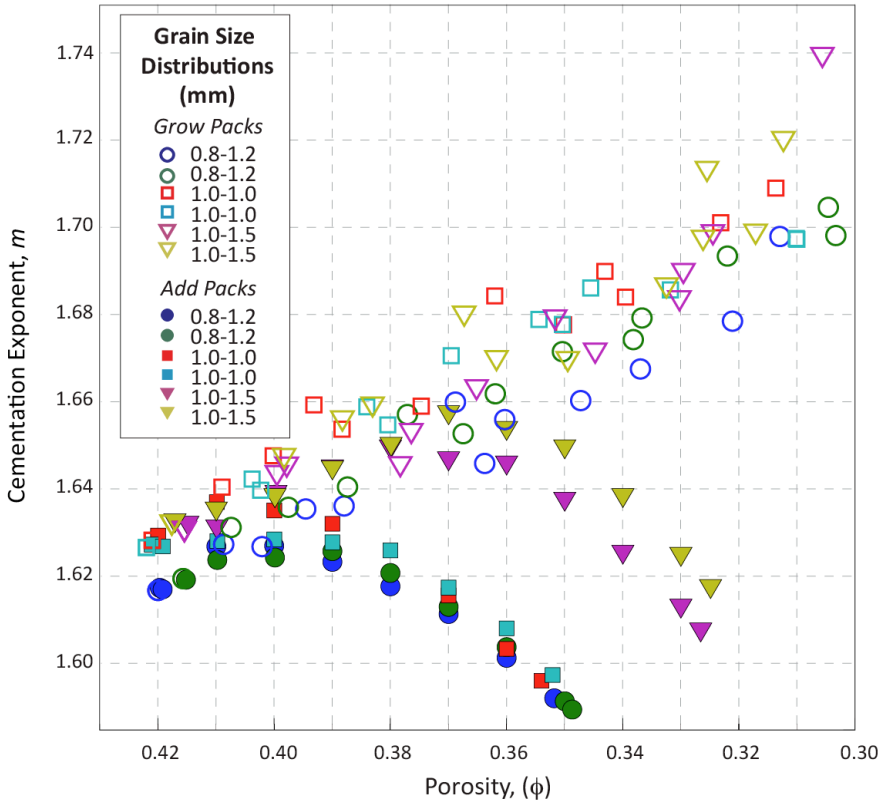

Figure 2-9: Cementation exponent calculated for six random packs using Add and Grow algorithms to decrease porosity.

The data from the pack perturbation algorithms was also analyzed with regards to bulk EC normalized by the fluid conductivity (Figure 2.10). The Add algorithm creates packs that are more conductive than the Grow algorithm. There are two approximate separation points from the Grow algorithm, which are related to average grain size. The first separation is at a porosity of ~0.40 for the grain packs with average diameters of 1.00mm, and the second at ~0.37 for the packs with average diameters of 1.25mm. These separation points are the same as seen in the previous analysis. The pack perturbation results were sorted into three groups: Grow Algorithm, Add Algorithm with an average grain size of 1.25mm, and Add Algorithm with an average grain size of 1.00mm. These

three groups were fit best by a quadratic relation; with linear and Archie relations also being examined. The median Archie Relation's (Archie, 1942) shape is shown for comparison; over this porosity range, changing the cementation exponent (*m*) acts to move the relation up and down without changing the shape significantly. It is interesting to note that a linear relationship also fits the data better than the Archie fit over this porosity range. It should be noted, however, that only the cementation exponent was varied when fitting the data with Archie's law. Other empirical constants have been used in the literature to increase the fitting ability of Archie's law, including a multiplicative scaling factor, *a*; this was not used in our analysis.

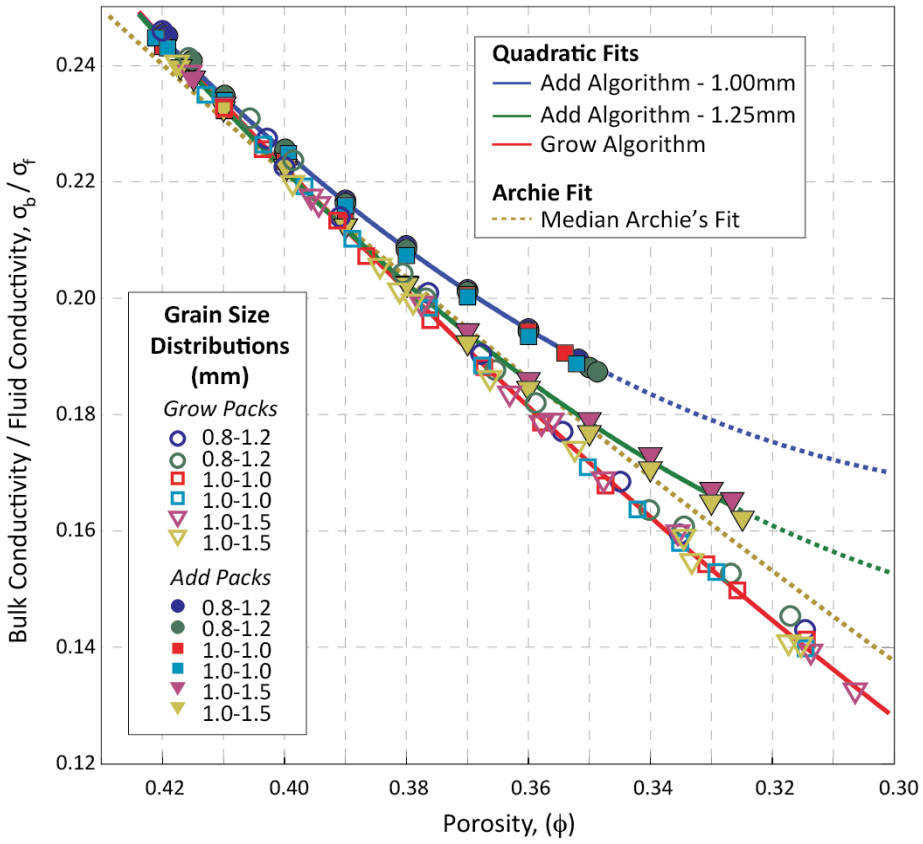

Figure 2-10: Normalized EC calculated for six random packs using Add and Grow algorithms to decrease porosity; the median Archie fit and quadratic relations are also shown for the three groups.

The differences observed in the electrical response are attributed to the pore space configuration, which was manipulated. Two measures for this configuration, in addition to porosity, are specific surface area and tortuosity. The changes in specific surface area for the two pack perturbation algorithms are seen in Figure 2.11. It was observed that the

higher the average grain size, the lower the specific surface area; this may help to explain the grain size specific differences within the Add algorithm seen in Figures 2.9-2.10. The Add algorithm increases surface area as it decreases porosity because it adds non-overlapping spheres in the pore space. The Grow algorithm decreases surface area with porosity reductions because it increases the radii of grains, and produces overlapping spheres with less total surface area. It was observed that EC response scales with specific surface area as well as porosity. However, the differences between Add and Grow are best captured by specific surface area calculations, which are sensitive to the specific pore configurations.

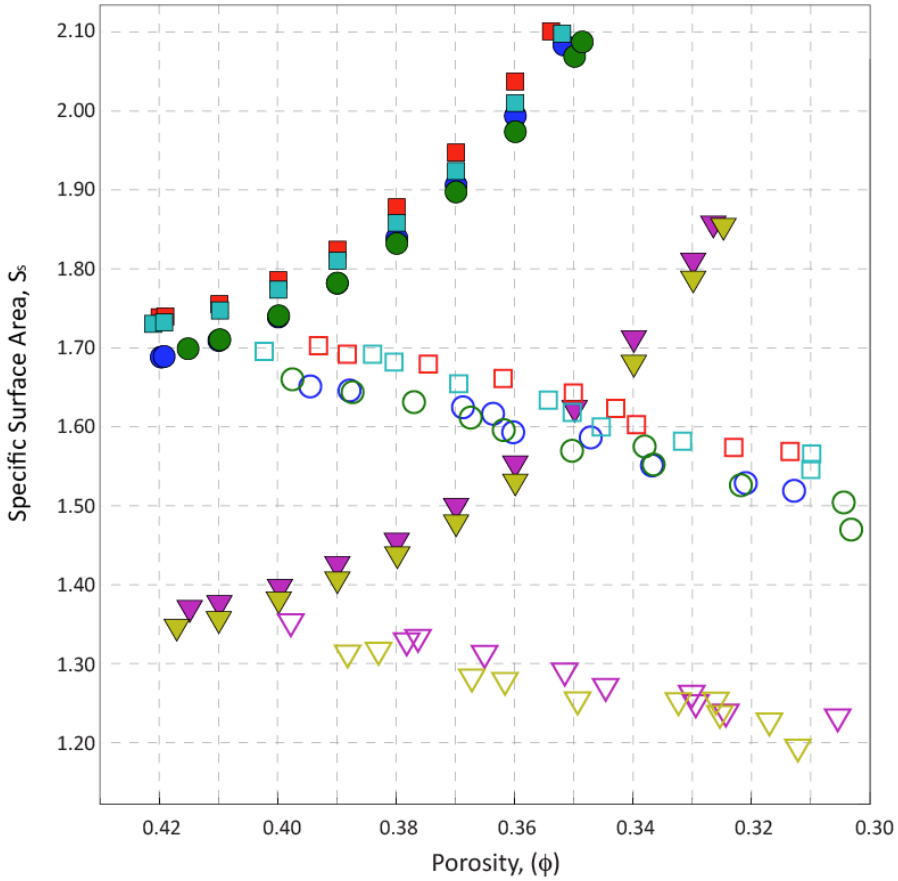

Figure 2-11: Specific surface area response under porosity reduction algorithms Add and Grow; the same legend is used as Figure 2.9: Add symbols are shaded, Grow symbols are open.

Electrical tortuosity is another measure of pore configuration, and thus was explored for differences between the Add and the Grow algorithm. Literature values for tortuosity distributions are not common, however, two simple theoretical equations for

tortuosity were found that were independent of Archie type parameters: $\tau = \left(\frac{(3-\phi)}{2}\right)^2$ and $\tau = \phi^{-1/4}$ (cited in Spearing & Matthews 1991). For a simple cubic pack ($\phi = 0.4764$) these equation yield tortuosity values of 1.6 and 1.2 respectively. The simple cubic pack in this numerical model provided an average tortuosity of 1.015, which is significantly lower than the range cited. This discrepancy can be explained by the type of tortuosity calculated, the tortuosity range above approximates a hydraulic tortuosity distribution; the numerical model implemented here uses the gradient of the electrical potential field to calculate tortuosity, and is thus sensitive to electrical tortuosity. In the simple cubic pack there is a straight line path through the center of the pores, and thus the electrical tortuosity, which contains no viscosity term, will be very close to this straight line path. Other tortuosity equations in the literature that rely on Archie parameters are see in Table 2.1. Using these equations and calculated Archie parameters to estimate electrical tortuosity yields a range of 1.28 to 1.75 for the unperturbed random packs. Shackelford (1991) presents a literature ranges for tortuosity in saturated unconsolidated sediment between 1.09 and 10.0. Electrical tortuosity is very much a theoretical concept that has not been rigorously defined and may be impossible to actually measure in a lab situation. The average electrical tortuosity plotted against the porosity for the Add and Grow algorithms is seen in Figure 2.12. The average electrical tortuosity of the unperturbed random packs (~1.09) was higher than the simple cubic pack, but was still low compared to empirical literature values.

As seen in Figure 2.12, there is slight separation within both Grow and Add based on average grain diameter (1.00mm and 1.25mm diameters), with the larger grain diameters having higher average electrical tortuosity values; this is especially evident in Add. Larger grain size distributions yielding larger electrical tortuosity values is related to the surface area of the spheres, or in the two-dimensional case the perimeter of the circles (Figure 2.14). It was observed that tortuosity scales with specific surface area, with more surface area being correlated with shorter possible pathways, and therefore less electrical tortuosity. In Figure 2.14 it is seen that although both schematics have the same porosity, the surface area is much greater in the Add algorithm. This additional

surface area allows for shorter possible pathways, and thus a smaller electrical tortuosity in the packs created by the Add algorithm, compared to the Grow algorithm. The original particle path for the unperturbed pack is shown in yellow in Figure 2.14; Add only modifies this path in the middle, while the path increases with the diameter of both grains in Grow.

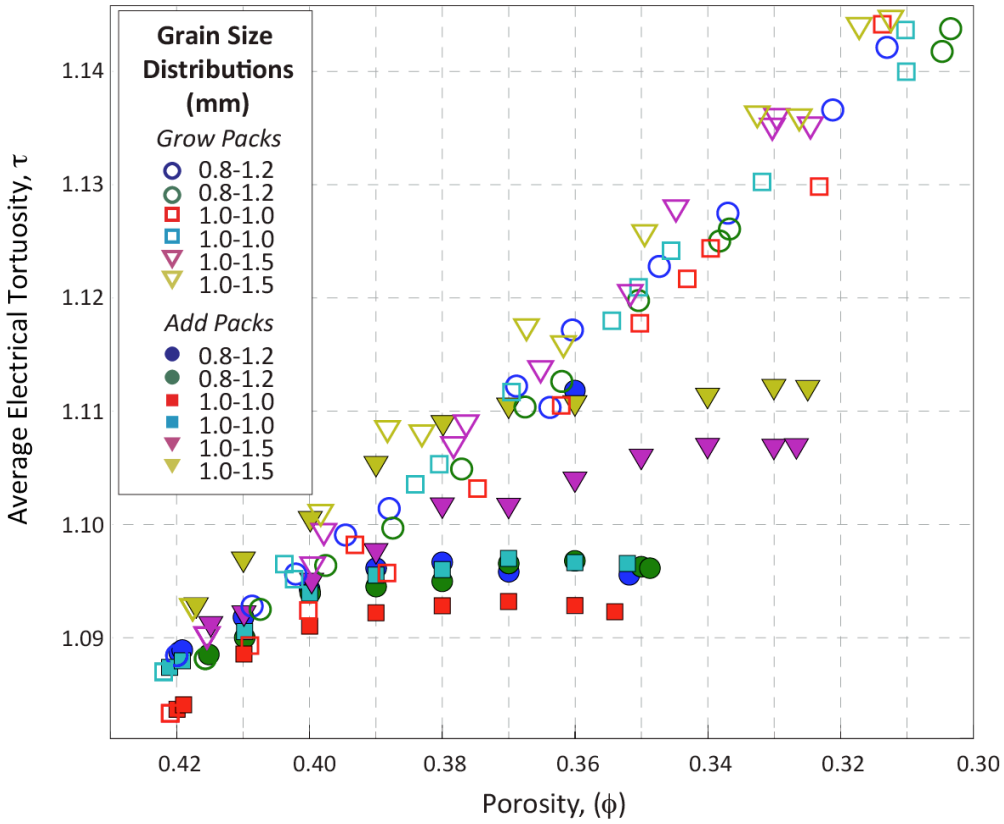

Figure 2-12: Average electrical tortuosity response under porosity reduction algorithms Add and Grow.

The normalized bulk EC of the grain packs is plotted against average electrical tortuosity in Figure 2.13. The EC of the packs decreases with increasing tortuosity in the Grow packs in a almost linear fashion. In the Add packs the tortuosity ceases to decrease at 1.10 and 1.11 for the 1.0mm and 1.25mm average grain size distributions, respectively (Figure 2.13). The bulk EC of the Add packs continues to decrease at these tortuosity values; this decrease is likely due to the reduction of conductive fluid and the addition of non-conductive grains.

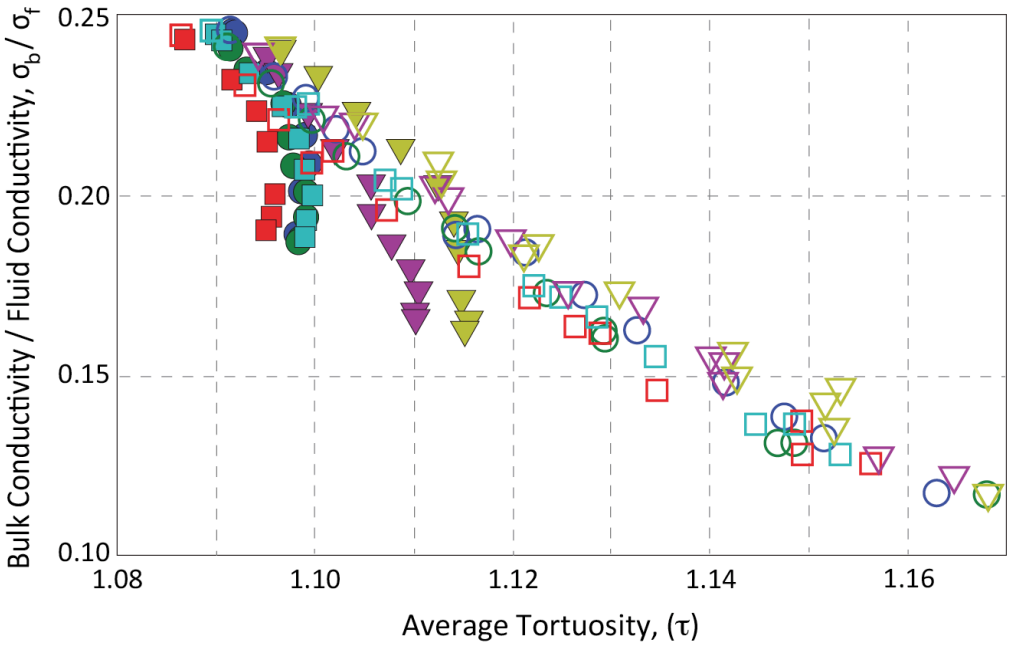

Figure 2-13: Normalized electrical conductivity plotted against electrical tortuosity under porosity reduction algorithms Add and Grow; the same legend is used as Figure 2.9: Add symbols are shaded, Grow symbols are open.

As the porosity of the random packs was reduced by the Add and Grow algorithms it was observed that the average electrical tortuosity increased over small porosity reductions (Figure 2.12). As the algorithms continued to decrease porosity, the electrical tortuosity response between the two algorithms differed. The two approximate separation points (0.40 and 0.37) between the two algorithms were again observed in the tortuosity response. The differing separation points in the Add algorithm were related to larger tortuosity associated with the larger grain sizes. The Grow algorithm acted to increase electrical tortuosity with decreases in porosity, this increase is due Grow having the greatest effect on pore throats, which necessarily lengthens electrical flow paths. The Add algorithm, which effects pore bodies, does not lengthen flow paths to the same extent as the Grow algorithm (Figure 2.14). This difference in pore manipulation in the two algorithms results in a very different electrical tortuosity response. While the Grow algorithm increases tortuosity with reductions in porosity, the Add algorithm results in initial increases that lessen as the algorithm continues; the average electrical tortuosity then stops increasing with decreases in porosity, and in some cases tortuosity decreases.

The decreases in electrical tortuosity are thought to be due to a numerical artifact of the tortuosity calculation. The approach used is not able to calculate path lengths with extreme curvature, as these paths have a higher probability of entering a grain and being discarded. Although the exact nature of the tail ends of the Add algorithm tortuosity calculation for the random packs cannot be trusted, the trend of decreasing sensitivity to porosity reductions is reasonable.

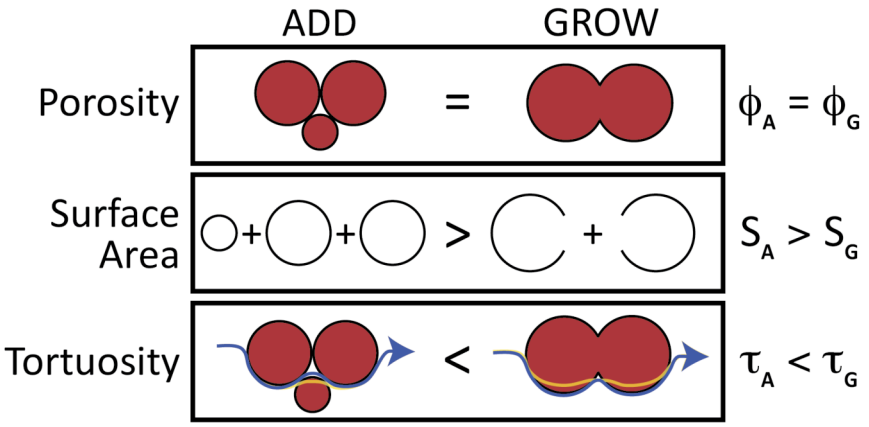

Figure 2-14: Schematic of the Add and Grow algorithms explaining the differences in surface area and tortuosity; a sample particle path for each algorithm is seen in blue, with the original path shown in yellow.

Tortuosity is sensitive to average grain size, and the method with which porosity is reduced. The Grow algorithm has the largest effect on pore throats and with every iteration of the algorithm there is an increase in electrical tortuosity. The Add algorithm has the greatest effect on pore bodies resulting in initial increases in tortuosity, but the sensitivity decreases as porosity is reduced. When observed as a whole, electrical tortuosity plotted against porosity is similar to normalized EC suggesting that bulk electrical response normalized for fluid conductivity is correlated with electrical tortuosity. Bulk conductivity of the random packs tends to increases as the electrical tortuosity of the pack decreases. The exact relations between electrical tortuosity and normalized bulk conductivity are not yet apparent from this analysis of the modeled data, and further research is needed to quantify a specific relationship between the hydrogoelogic parameters.

2.6 Conclusions from the Numerical Model

The relative independence of EC from hydraulic conductivity was demonstrated for the ordered packs (simple cubic packing and hexagonal close packing) by reducing the grain size while keeping porosity constant. However, these conductivities are often correlated due to reliance on many of the same parameters.

The numerical model presented calculates Archie type electrical parameters that are in the literature range for unconsolidated sediment. Using the porosity reduction algorithms, which have the greatest effect on pore bodies in Add and pore throats in Grow, differences in electrical responses were studied. Porosity was reduced from 0.42 to 0.30, and over this range the numerical model calculated that Archie's cementation exponent, m, varied non-linearly between 1.58 and 1.74. This range is important when making interpretations at the field scale. Hydrogeologic parameters, including porosity, specific surface area, and electrical tortuosity, were used to investigate the difference in electrical response between the Add and Grow algorithms. Porosity and surface area calculations were robust, however, the tortuosity calculation broke down when multiple high curvature grain-fluid interfaces were introduced in the model space. It was found that electrical tortuosity scales with surface area, which is a more robust calculation. The differences in electrical conductivities found between the Add and the Grow algorithms can be explained by tortuosity, and in part by changes in specific surface area. These results demonstrate that the electrical resistivity response of these two porosity reduction algorithms have different functional relationships. Given these different rock physics relationships, it may be possible to distinguish these two mechanisms, in-situ, using high quality time-lapse electrical resistivity data.

2.7 Future Work & Contributions

To extend the research on pore scale modeling the current tortuosity calculation needs to be improved so that it can more accurately capture high curvature grain-fluid interfaces. It may also be illuminating to compare modeled electrical and hydraulic tortuosity by finding bulk hydraulic conductivity measurements. This may ultimately necessitate implementing the full Navier-Stokes equation. Using an alternate packing model to simulate sediment cores would be useful for observing porosity variations due

to grain configurations, rather than grain perturbations. Grain surface conduction is also of interest; this is especially prevalent in the biofilm modeling (Grow algorithm) because it is known that biological growth has significant surface or volume conductance (Atekwana *et al.*, 2006).

This work focused on developing and testing a numerical modeling approach that is useful for studying some of the limits of using EC to glean insight about in-situ hydrogeologic parameters. As a result of this numerical model: (1) I developed significant amounts of code that have many potential uses and applications (Table 2.2); (2) conceptual models of pore scale electrical processes, parameters, and relations were created; and (3) the utility of Archie's law was explored, including expected ranges and temporal variability. These conceptual models and possible limitations of empirical equations must be in place when analyzing field data. Harkins recharge pond shows temporal variability in the supposed constant formation factor, this numerical model has determined that changes in porosity and pore geometry can cause this variability.

Table 2.2: Titles and explanation of code developed in Matlab for this numerical model.

Code Title	**Description**
Pack Discretization Algorithm	- Creation of a 3D model given locations and radii of sphere. - Addition of electrical conductivity values - Addition of electrical end plates
Add Algorithm	- Numerical and analytical identification of non-overlapping spheres - Addition of spheres to 3D model to a set porosity
Grow Algorithm	- Random increase of grain radii in 3D model - Porosity calculation at every iteration
Surface Area Calculation	- Analytical calculation of surface area for simple grain to gain overlaps - Numerical calculation of surface area for complicated grain overlaps - Volume calculation
Particle Tracking Algorithm	- 2D and 3D particle tracking algorithm given a potential field. - Calculation of particle path lengths.
Ordered Pack Algorithms	- Creation of sphere locations for the two ordered packs considered: - Simple Cubic Pack - Hexagonal Close Pack
Visualization Code	- Visualization techniques using Matlab software for: sphere packs, numerical models, surface area calculation, and particle paths.

Chapter Three: Field Inversion

3.1 Field Acquisition

EC measurements were collected to glean information about the hydrogeologic processes in the subsurface of Harkins Slough in California. To monitor and research these processes, four permanent probes were installed in the water column and in the top two meters of the aquifer for the January 2008 to May 2009 infiltration season (Figure 3.1). These probes can be used to measure EC and temperature, and are also able to retrieve water samples along the length of the probe. A schematic of an EC probe is presented in Figure 3.2. High-resolution EC measurements are taken over the entire length of the infiltration. The information from the probes has many potential uses including: identifying the cause of decreased infiltration; creating saturation and porosity models over time; helping to calibrate hydrogeologic flow models; and researching some of the finer details of the link between electrical conductivity and pore water quantity, quality, and connectivity.

We designed and built these probes in-house at the University of Calgary during August and September of 2008. As part of this research, I managed the assembly of the probes, which involved integrating the temperature sensors into the probe body and building in the wired electrode assemblies. The probes were designed to allow emplacement using a direct push drill rig (e.g. geoprobe). Using this method of emplacement minimizes disturbance to the material immediately adjacent to the probes as well as the potential for creating preferential flow paths down the length of the probe.

The EC probes are spaced approximately 20m apart in the pond (Figure 3.1). These probes were 3m long and were installed to a depth of 2m through a combination of drilling and direct push to maximize contact with the surrounding sediment. A steel rod, which was 2/3 the diameter of the EC probe, was pushed in before the probes to reduce the force required for pushing in the probes. This steel rod was pushed ~15cm deeper than the maximum depth of the probe to accommodate for sluffing of unconsolidated sediment from the side of the predrilled hole. Consequently, this location directly beneath the probe may have higher porosity than the surrounding sediment. The probes were then pushed into the sediment using a direct push rig until the highest subsurface electrode

was beneath the ground. The probes have 25 electrodes at 10cm intervals monitoring the subsurface and four electrodes ~1m above the ground surface at the same spacing. The electrodes above ground are able to measure fluid conductivity when covered with water. The probes were designed to take fluid samples at multiple locations along the length of the probe, this feature was somewhat hindered by unforeseen saturation variability. Temperature measurements were taken using thermistors, which are calibrated resistors that are sensitive to temperature variations. The data for direct fluid measurements and temperature readings are not presented here, as they are not part of this investigation.

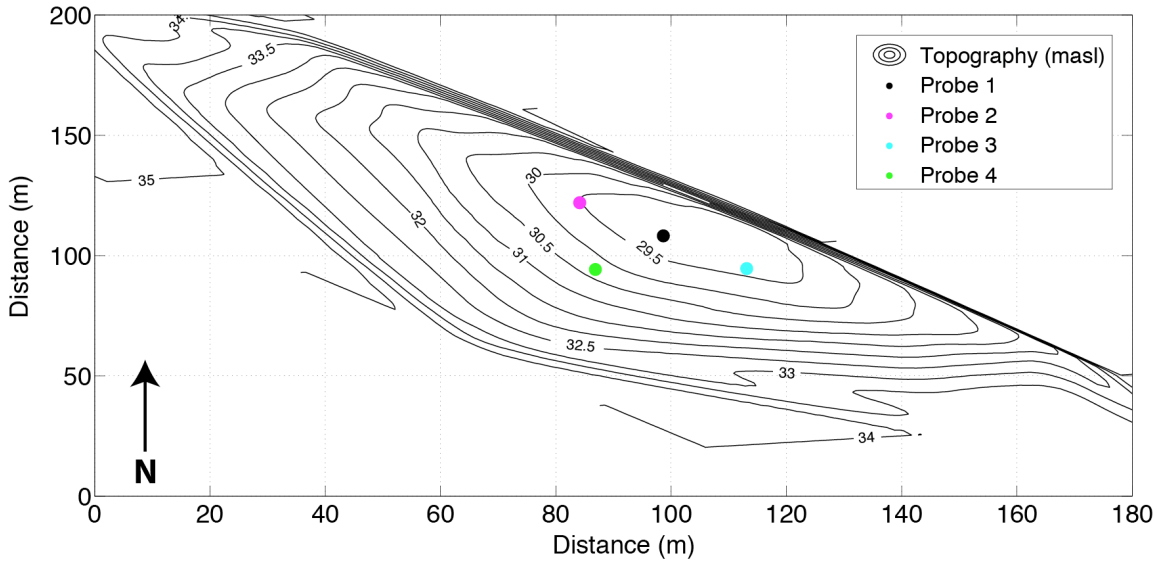

Figure 3-1: Topography map of Harkins recharge pond showing the locations of the EC probes.

The acquisition sequence of the electrical conductivity probes combines multiple types of arrays. The Wenner and dipole-dipole arrays, illustrated in Figure 1.1, are sampled for all possible combinations in the vertical probe. Additionally, a multitude of overlapping electrical measurements are taken such that the electrical conductivity data can be inverted and more detailed EC estimates of the subsurface can be made. These measurements are taken approximately every 18 minutes for the length of the experiment, yielding a detailed and comprehensive data set of 9685 time measurements for each of the four probes. However, in Probe 1 there was a problem with the wiring and the recorded data were scrambled; thus, Probe 1 was not used in this analysis. The data from the probes is stored in and uploaded from a watertight container on the north-east side of

Harkins recharge pond. The electric and computer system, contained in this box, went down in the 2008-2009 field season for about a week after a storm; this resulted in a loss of data while the pond was being filled.

3.2 Inversion of Conductivity Data

A version of RESINVM3D, written in cylindrical coordinates was used to invert the probe data. The code was used in a mode that assumes radial symmetry. Radial symmetry was invoked because all of the data where acquired along a single axis and there is therefore there is no information in the data about the angular direction of an anomaly. The assumption of radial symmetry is such that the inversion results, while presented as a 2D plan, in terms of radial distance and depth, actually correspond to a series of "rings" around the probe. An illustration of one of these cylindrical cross sections is shown in Figure 3.2.

3.2.1 Model Grid

A finite volume grid was chosen that allowed fine discretization near the probe with increasing grid spacing moving away radially and with depth. This grid spacing allows for high amounts of sensitivity close to the probe where electrical conductivity measurements are taken. Two of these finite volume grids were created for each model, an inversion grid and a computational grid; the inversion grid was coarser than the computational grid by approximately a factor of five. The computational grid is used for calculating the forward response of a given conductivity distribution, while the inversion grid is used for recovery of the unknown resistivity structure. The computational grid is refined so as to produce a more accurate solution to Possion's equation. The inversion grid is coarser than the computational grid for two reasons: 1) the coarser grid is more consistent with the information content of our data, and 2) the coarser grid makes the inversion calculation more computational efficient. A portion of the inversion grid is shown in Figure 3.2. The model space for the inversion grid is 28 m wide for all inversions; the first four cells in the radial direction are less than 5cm wide; the radial grid dimensions then increase by a factor of 1.2 to a maximum dimension of 1.15m. The model depth is variable with the height of the water column in the pond; however, the subsurface depth dimensions remain constant. Beneath the ground surface, the inversion

grid has constant dimensions of 5cm for the first 3m; the depth dimensions then increase by a factor of 1.2 to a maximum dimension of 1.92m. The grid choices allowed a compromise between computational time and approximating boundaries at an infinite distance from the probe.

3.2.2 A priori Knowledge

As seen in Eq. 1.8 the RESINVM3D contains multiple terms (e.g. β, $\mathbf{W}$, and $\mathbf{m_{ref}}$) that allow for inclusion of *a priori* knowledge. As with most deterministic inversion codes there is an option to apply smoothness and smallness (relative to a reference model). In particular, smoothing can be independently controlled for the radial and vertical directions. Both smallness and smoothness can be controlled in a global sense (i.e. across the entire model space) through global parameters, or they can be tweaked for individual cells by adjusting a model weighting matrix. The model weighting matrix is particularly important when one has a-priori information about discontinuities (e.g. location of a water boundary), as it allows the user to reduce, or increase, regularization in a given region of the model. Furthermore, model weighting can be used to enforce soft constraints, such as known conductivity values. For a large weighting parameter, the inversion will be forced to stay close to the starting model in a given area. This can also be achieved in the "hard" sense by making a given model cell inactive (i.e. inactive cells are not updated in the inversion). A data weighting matrix was used that was weighted inversely proportional to the magnitude of the voltage measurement. The inversion program also allowed for the smoothing constraints to be turned off at boundaries of choice. The boundary between the water and the sediment is known, and according to Archie's law (Eq. 1.9) there is a difference between water EC and saturated sediment EC. The water-sediment boundary was enforced to not be smooth for a portion of the inversions ran.

In addition to smoothing, introducing a-priori knowledge, by way of a complicated starting model, is a particularly useful way to constrain the inversions. In this work we explored, among other things, the inclusion of a thin conductive layer adjacent to the probe to investigate effects due to conduction or preferential fluid flow paths along the probe.

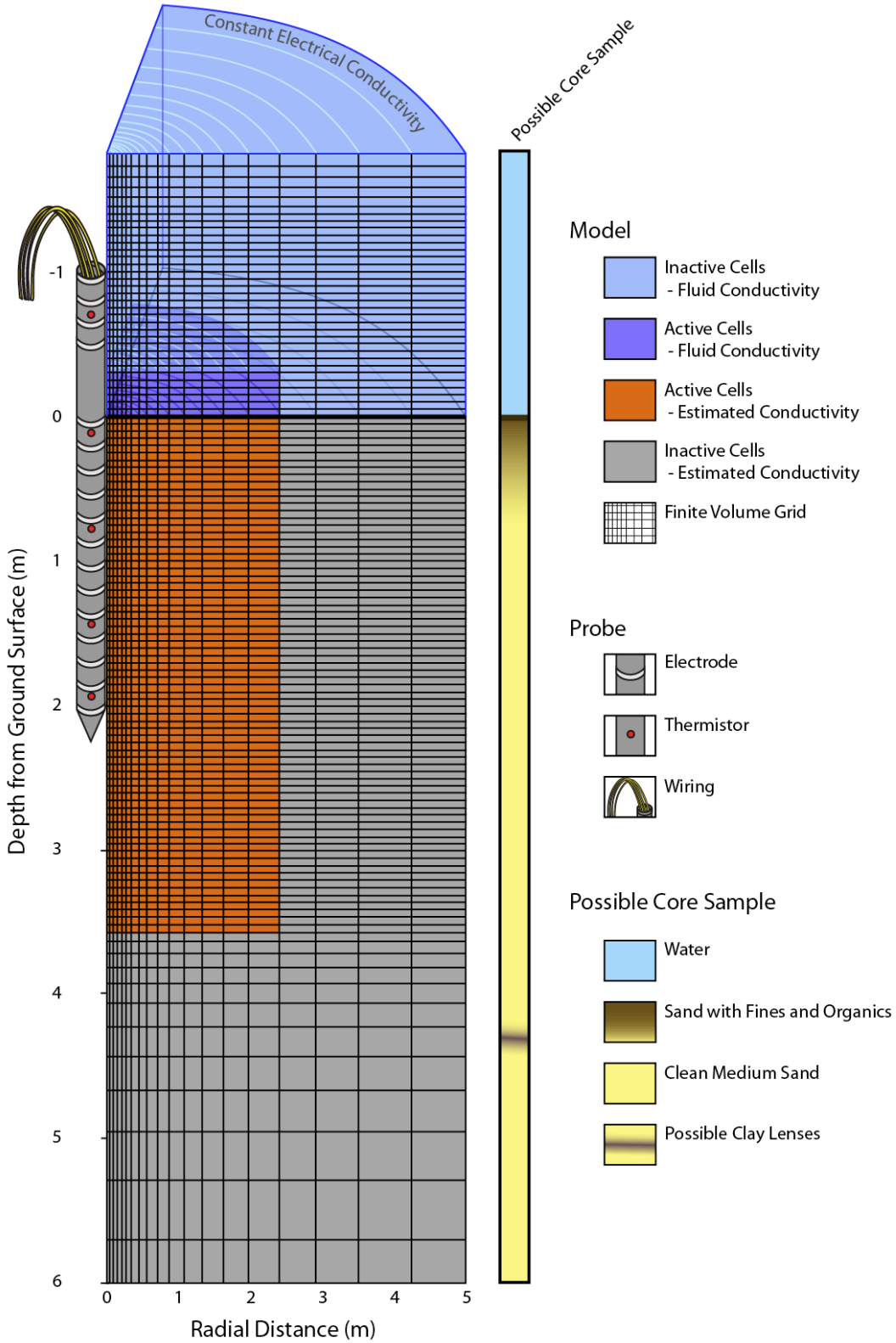

Figure 3-2: Schematic of probe installation, possible core sample showing sediment location, finite volume grid, cylindrical coordinates, and sample model geometries used for the Ref_N.nS.W inversion.

3.2.3 Iterations and Tolerance

The number of iterations needed for each model varied with the reference model provided, with better initial reference models (m_{ref}) requiring less iterations. The maximum number of iterations was set to eight; however with good reference models the inversion ran below misfit tolerance in 3-5 iterations. The inversion misfit tolerance was set to 0.5% and represented the l^2-*norm* of the difference between the observed data and the modeled data.

3.3 Water Column Height and Conductivity

Both the water column height and the EC varied with time in the experiment. The pond was dry during the installation of the EC probes in December 2008, which is defined as time 0. Figure 3.3a shows the height of the water column above each of the three probes. As electrical conductivity is sensitive to changes in both fluid conductivity and saturation (Archie, 1942) the accurate measurement of the water column is an important piece of information. The water height was calculated using external data from a pressure transducer in the bottom of the pond. This universal water column data had to be calibrated to each specific probe elevation for inclusion in the inversion.

The water column height data shows that approximately 13 days after the probes were turned on there was a rain event, this partially filled the bottom of the pond; water persisted in the pond for a week. Following the first major storm of the winter (at 48 days) the pumps were turned on, filling the pond to a depth of ~3m. The pumps were then shut off because the water from Harkins Slough was too turbid to be suitable for infiltration; this is seen as a decrease in the water column height at ~54 days. Pumping was resumed once the turbidity in Harkins Slough was reduced, and the pond height was raised to ~5m. The missing data between 62 days and 69 days is due to equipment failure. Figure 3.3b shows the measured EC of the water column over the length of the experiment. The water height rose above the water column electrodes shortly after the pumps were turned on. The EC is measured by a Wenner and a dipole-dipole array in the water column and averaged. The EC of the water from the first storm of the season was the highest seen over the experiment. This is expected because the first storm of the

season mobilizes fine sediments and dissolves fertilizers and salts from agricultural fields. This water had a higher portion of dissolved and suspended load than later in the season, and thus a higher EC. Water used later in the experiment had a smaller dissolved load and was relatively constant. However, the EC of the water column rises over the rest of the infiltration experiment. EC is sensitive to temperature variations and increases 1.87% per 1°C (Hayashi, 2004). The increases seen over time in the EC of the water column (80-130 days) are primarily due to atmospheric forcing in the form of seasonal temperature increases.

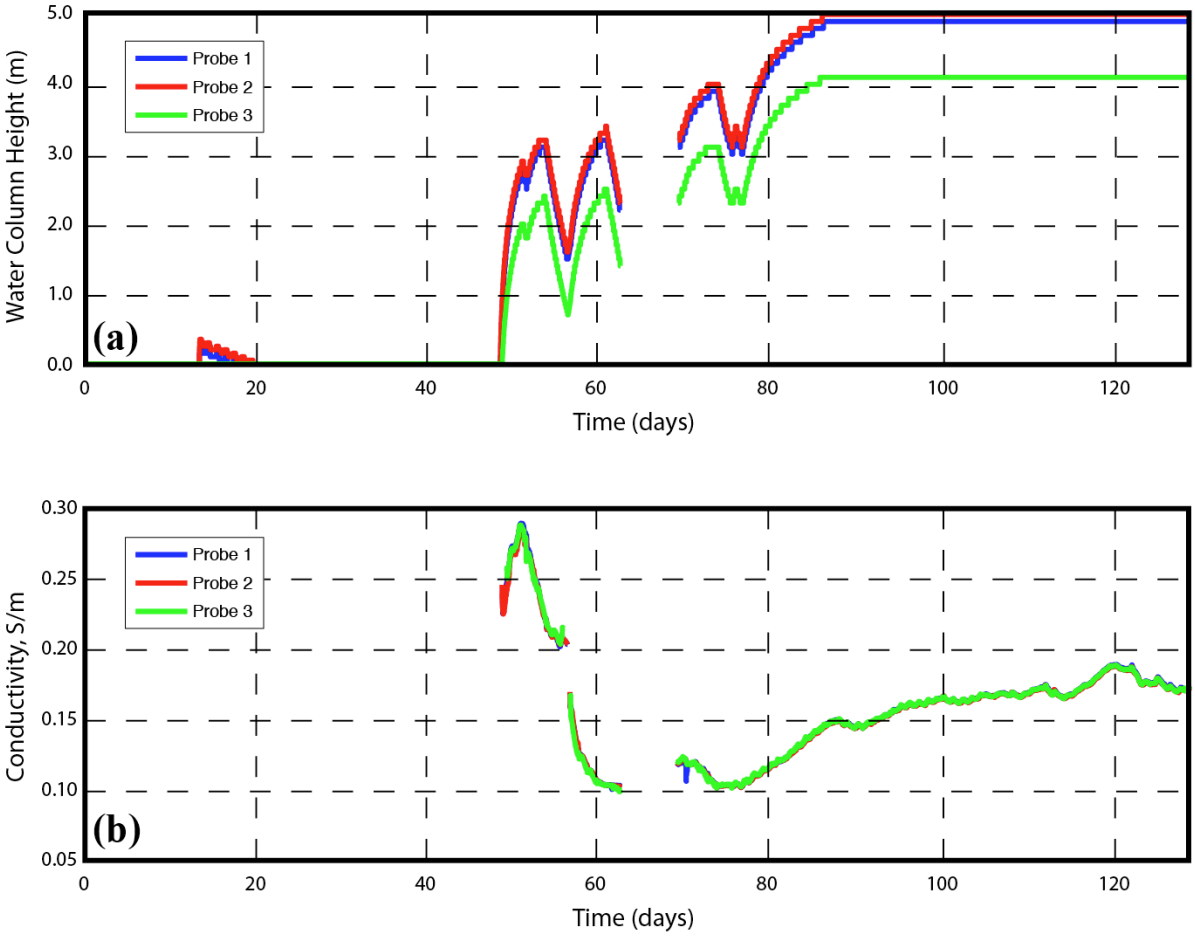

Figure 3-3: Changes in (a) water column height; and (b) EC of the water column over time at Harkins recharge pond.

3.4 Inversion Methods

The EC data recorded in the subsurface was inverted using six different methods; these are summarized in Table 3.1. The Homogeneous method was used to determine

what the inversion program would conclude given no *a priori* information. The Homogeneous inversion method used the average apparent conductivity of the sediment for each data set as the reference model; all cells were allowed to be active. This method indicated that there was a more conductive layer against the length of the probe as well as a conductive volume at the very tip of the probe. It was thought that the conductive layer against the length of the probe was due to a combination of probe conduction and preferential flow of water against the probe. The conductive area at the tip of the probe was thought to be the possible high porosity volume artifact from the probe installation. For all of the subsequent inversions the same process was used to create the reference model with only minor changes. This reference model was created using the apparent conductivities calculated from all EC measurements. These apparent conductivity values were placed at the vertical midpoint of the measurement and radially offset from the probe depending on the spacing of the measurements, with close spacing having zero offset. The resulting scatter plot was then linearly interpolated to fill the entire model space. Additionally, for the rest of the inversions the active cells, which were allowed to be changed by the inversion program, were limited: radially to within 2m of the probe; and vertically from a maximum depth of 3.5m (1.5 m below the probe) to 30cm into the bottom water column, if water was present. This volume is shown schematically in Figure 3.2. The next inversion that was run, Ref_C.S, overwrote the closest radial cell along the length of the probe with a conductivity of 0.035S/m; this was ~1/3 of the average fluid conductivity (Table 3.1). Figure 3.4 shows the inversion error (data misfit) over the length of the experiment for the inversion methods (b)-(f). It was found that for Probe 3 reference model Ref_C.S was accurate to within 0.5% of the observed data after the pond had been filled. However, this inversion method produced 1.5-3.0% error when the pond was dry (Figure 3.4). Additionally, in Probe 2 when the pond was filled, there was ~1.5% inversion error. The conductive layer along the probe was taken out in Ref_N.S and the standard reference model was used (Table 3.1). This reference model created inversions that had less than 1% inversion error over the entire infiltration experiment; there was more error once the pond was filled (Figure 3.4). For the next three inversion methods, the smoothing gradient at the water/sediment interface was turned off

allowing for a jump in the conductivity values at this boundary (Table 3.1). Ref_C.nS had the conductive layer along the length of the probe and was not smooth at the water/sediment interface. This inversion method was very similar to Ref_C.S but produced lower inversion error when the pond was filled with water; the final iteration error was still higher than the inversion tolerance for the majority of the experiment length (Figure 3.4). Ref_N.nS used the standard reference models and the smoothing constraint over the water/sediment boundary was turned off (Table 3.1). This method was very similar to Ref_N.S with all inversions having less than 1% error (Figure 3.4).

Table 3.1: Summary of the six inversion methods used to invert the time-lapse data.

	Inversion Name	Reference Model	Conductive Along Probe	Active Cells	Not Smooth at Ground Surface
(a)	Homogeneous	Homogeneous using the average sediment conductivity		All	
(b)	Ref_C.S	Apparent conductivity model measured by the probe Conductivity along probe increased to 0.035S/m	✔	Vertical: -0.3 to 3.5m Radial: 0 to 2m	
(c)	Ref_N.S	Apparent conductivity model measured by the probe		Vertical: -0.3 to 3.5m Radial: 0 to 2m	
(d)	Ref_C.nS	Apparent conductivity model measured by the probe Conductivity along probe increased to 0.035S/m	✔	Vertical: -0.3 to 3.5m Radial: 0 to 2m	✔
(e)	Ref_N.nS	Apparent conductivity model measured by the probe		Vertical: -0.3 to 3.5m Radial: 0 to 2m	✔
(f)	Ref_N.nS.W	Apparent conductivity model measured by the probe. **Water column overwritten by fluid conductivity.**		Vertical: -0.3 to 3.5m Radial: 0 to 2m	✔

Ref_N.nS.W used the standard reference model, but overwrote the entire water column with the fluid conductivity value (Table 3.1). If a fluid conductivity was not available, this method uses the nearest neighbor. This inversion method produced the least inversion error over the entire experiment; errors were consistently below tolerance when the pond was filled (Figure 3.4). There are two isolated times in this method where errors are ~2%: the rain event, and the very beginning of the infiltration experiment; these are due to poor constraints on the fluid conductivity (Figure 3.4).

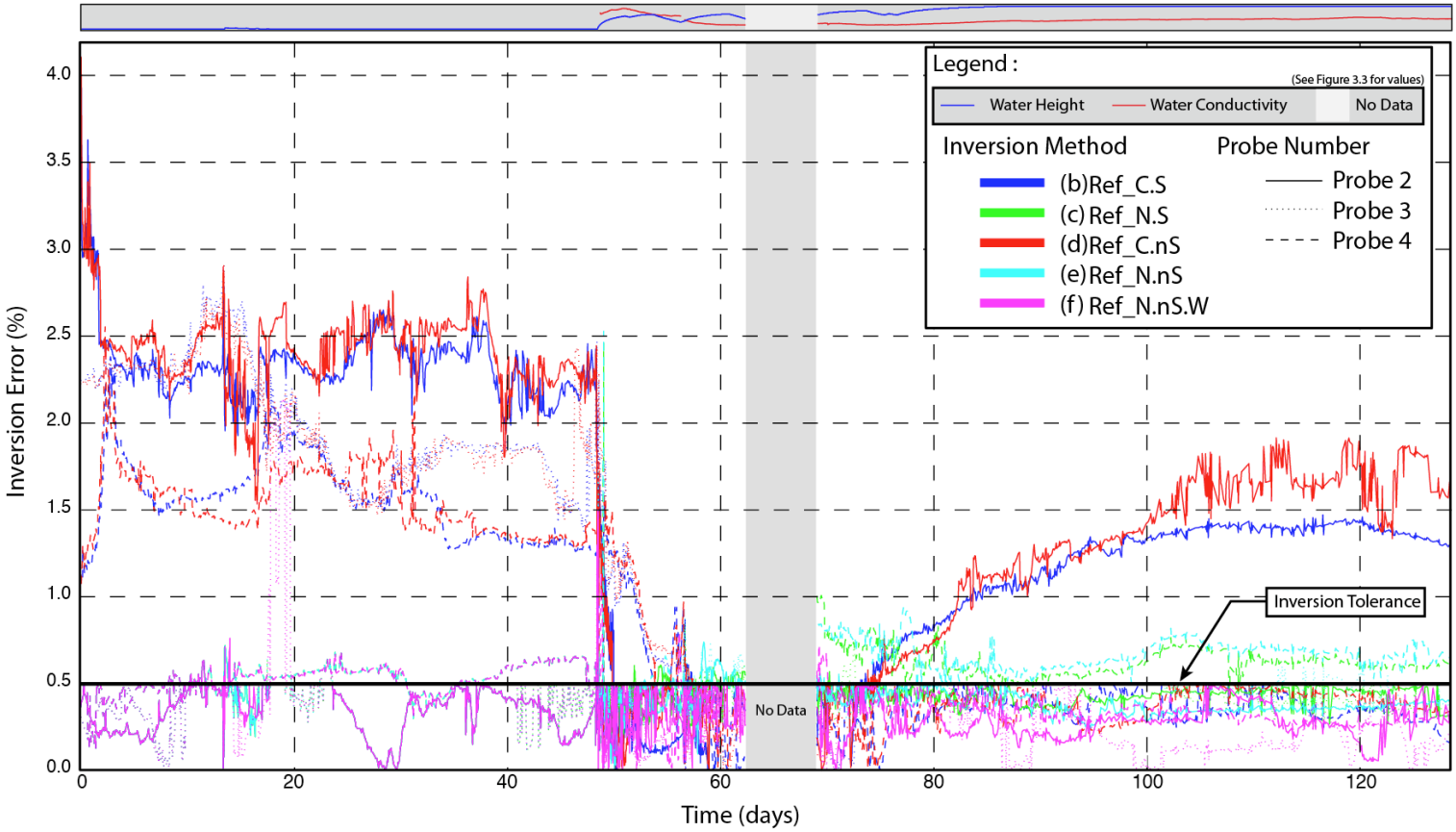

Figure 3-4: Inversion error over time for five of the inversion methods; water column height and EC are plotted above for reference purposes.

3.5 Inversion Results

The inversion results over time for the six inversion methods are seen in Figures 3.5, 3.7, and 3.8 for Probes 2-4 respectively; these six methods are described in Table 3.1. The figures show the estimated log conductivity of the top two meters of the sediment 35cm radially away from the probe. Additionally, an illustration of water column height and EC

is shown above each inversion for reference purposes. In these figures hot colors represent high conductivity values and can be generally interpreted to be wet; and cool colors represent low conductivities that can generally be interpreted as dry. From Archie's law (Eq. 1.9) it is known that EC is empirically related to saturating fluid EC, porosity, and saturation; an increase in any of these parameters acts to increase EC. In Probe 2 the top 50cm show the most variability in EC (Figure 3.5). Before infiltration begins there is a high EC area to a depth of 17-22cm in all inversions except the Homogeneous run. The EC of this area increases after the rain event; this increase in EC is best seen in Figure 3.5 (b) and (d). The depth of the high EC area increases to 40-50cm when the pond is filled, and likely represents a change in saturation. After the pond has been filled, the top 50cm decrease in conductivity and then show slight increases; these increases are best seen in Figure 3.5 (c) and (f). This EC pattern in the top 50cm after the pond was filled is a dampened and lagged response to changes in the water columns EC (Figure 3.3). Below the top 50cm of the profile there is a dampened response to all changes in the pond. The rain event is seen in all inversions, but is most prominent in (c), (e), and (f) and seen as an increase in conductivity that persists for a week. Directly after the pond was filled (t = 48days), the area below 50cm has increases in EC that show a different pattern than in the top 50cm. Although there are initial increases in EC below 50cm depth, after day 80 there is not an increase in EC corresponding to seasonal temperature increases. This difference in response between the sediment above 50cm, which has increases in EC after 80 days, and below 50cm, which shows continued decreases, may indicate sensitivity to a different hydrogeologic parameter. The top 50cm are likely saturated, reducing Archie's law to dependence on porosity and fluid EC; of these two parameters, fluid EC will have the largest variability. Thus, variation in the EC response in the top 50cm is based primarily on fluid EC variability. Below 50cm it is thought that the area is not fully saturated at any time in the experiment; this interpretation is due to the two order of magnitude contrast in EC with the top 50cm. Assuming this layer is not saturated increases the complexity of Archie's law to dependence on saturation. The magnitude of saturation of this lower layer will determines whether EC is most sensitive to changes in fluid EC or slight changes in saturation. For

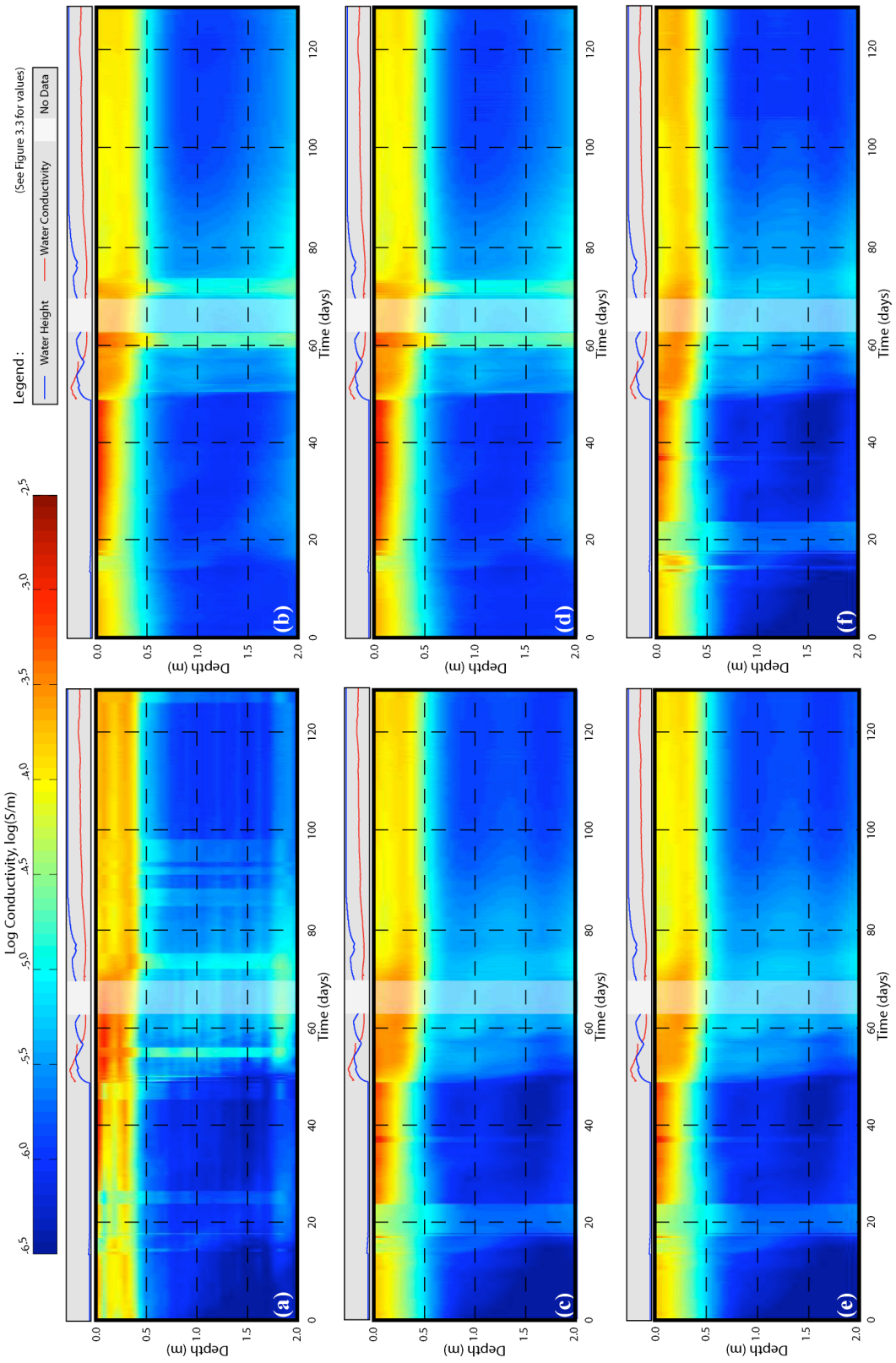

Figure 3-5: Probe 2 inversions shown in log conductivity; see Table 3.1 for descriptions.

example at low values of water saturations, EC will be most sensitive to slight changes in saturation. In Figure 3.6 Ref_N.nS.W is used to plot EC changes over time at various depths. The rain event is seen at all depths as seen in Figure 3.5, however, Figure 3.6 illustrates the discussed difference in response to the water column height and EC. At 0.25cm depth the EC profile mimics the water column EC showing an initial high followed by a decrease and then seasonal forced increase. At depths below 1m the EC response mimics changes in the water column height, with peaks in the EC lagging behind the water column height. Saturation is linked to infiltration rates, which are dependent on the pond depth at early times in the experiment, and thus there is a conceptual link between saturation of this area and the height of the water column. This dependence on the water column height indicates that saturation of this area is

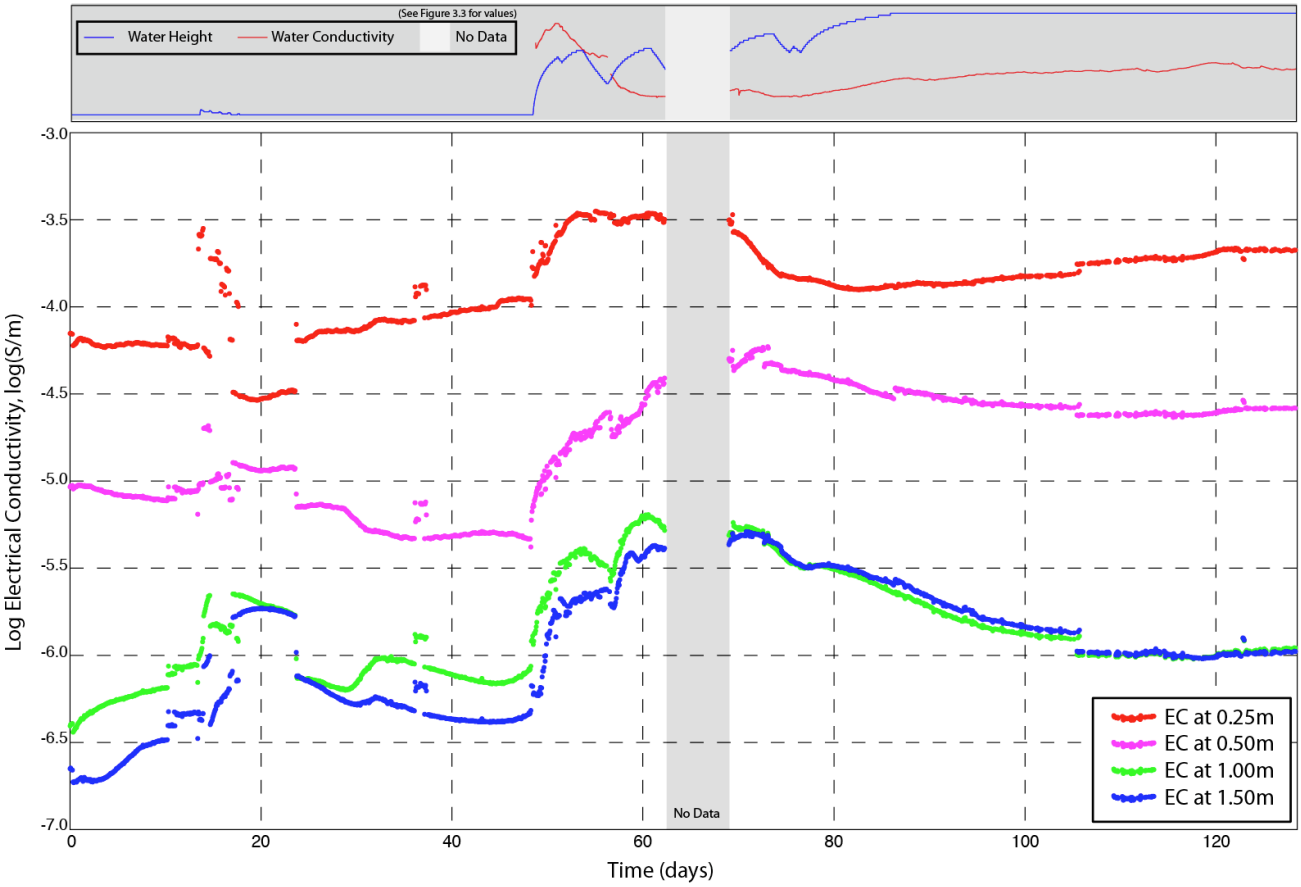

Figure 3-6: Electrical conductivity response at various depths using Res_N.nS.W for Probe 2 over time; the water column height and conductivity is illustrated for reference purposes.

sufficiently low enough to cause dependence on slight changes in saturation; this area is relatively insensitive to changes in fluid conductivity. It should be noted that the lag between the water column height and the inferred change in saturation cannot be used to determine a ground water velocity, as changes in saturation are linked to, but not directly correlated with, velocity. At a depth of 50cm, which is the approximate depth of the interface of these two saturation layers, the EC mimics patterns from both water height and fluid EC variations. The slight dependence of water column height suggests that water saturations are high but not 100%. The decreases in EC after 80 days in areas below 1m likely represents decreases in saturation; since the pond height and fluid EC remain relatively constant this decrease may correspond to pond clogging.

The inversion results for Probe 3 for the six inversion methods (see Table 3.1) are shown in Figure 3.7. These inversion images are similar to Probe 2, however, there is no distinct saturation boundary. In all of the six inversion methods there are jumps in EC between time steps; however, it is expected that changes in time are relatively smooth, with the exception of times where there is a significant change in water column height. These jumps in EC make the time-lapse interpretations difficult, as it is likely that there are numerical anomalies present in the inversion. Inverting all of the data at the same time instead of individually, and providing a smoothing constraint through time could address this problem. For Probe 3, it was found that forcing the layer of sediment along the probe to be more conductive than the surrounding sediment produced inversions with misfit errors below the inversion tolerance (Figure 3.4). It is seen in Figure 3.7 that these two models, (b) and (d), also produced the smoothest inversions in time. These two inversions indicate that conductivities increase at all depths after the pond is filled. This may indicate that saturation never decreases at depth or that the profile is saturated enough such that fluid EC dominates the response. The rain event seen in Figure 3.7 (b) and (d) acts to decrease the EC of the top 40cm while there is water in the pond. It should be noted that this is the only time the pond receives water from direct precipitation, and the water likely has a lower EC; the water from 50 days onward is pumped from Harkins

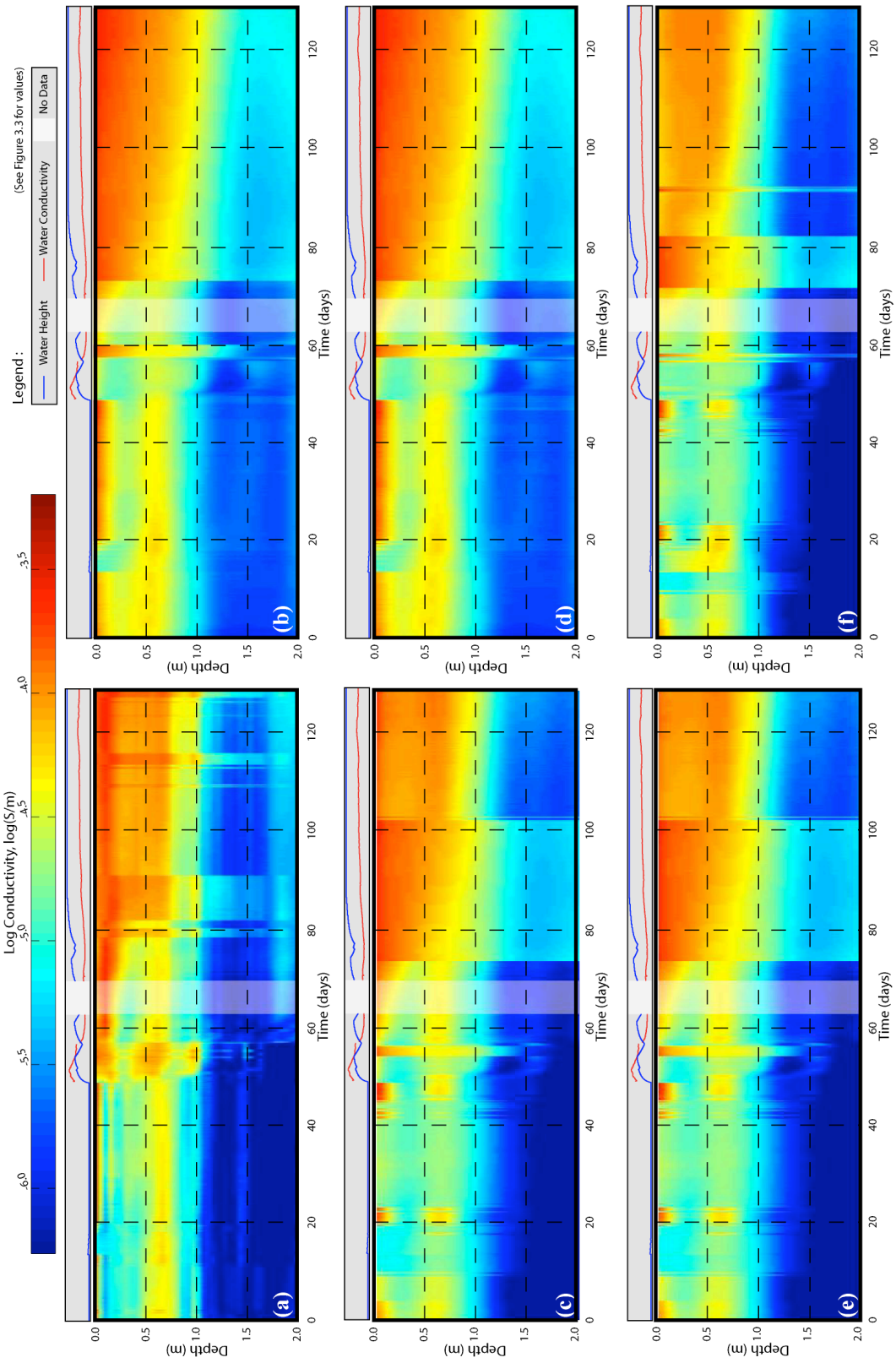

Figure 3-7: Probe 3 inversions shown in log conductivity; see Table 3.1 for descriptions.

Slough. After the rainwater height in the pond drops below the probe, the conductivity increases within a day; this increase in EC could be due to evaporation that concentrates pore fluids.

The six inversions for Probe 4 are shown in Figure 3.8. These inversions have few anomalous jumps in EC over time. Similar to Probe 3, there is no distinct saturation change inferred from the inversion data. Please note that the yellow 'boundary' pictured in Figure 3.8 does not represent a sharp change, and is just a visual artifact of the color scheme. All inversion methods except Homogeneous found that the EC of all of the sediment increased continually after the pond was filled; this corresponds to increases in saturation or fluid EC. It should be noted that no rain event is seen in this data, as the water column did not rise above this probe's elevation.

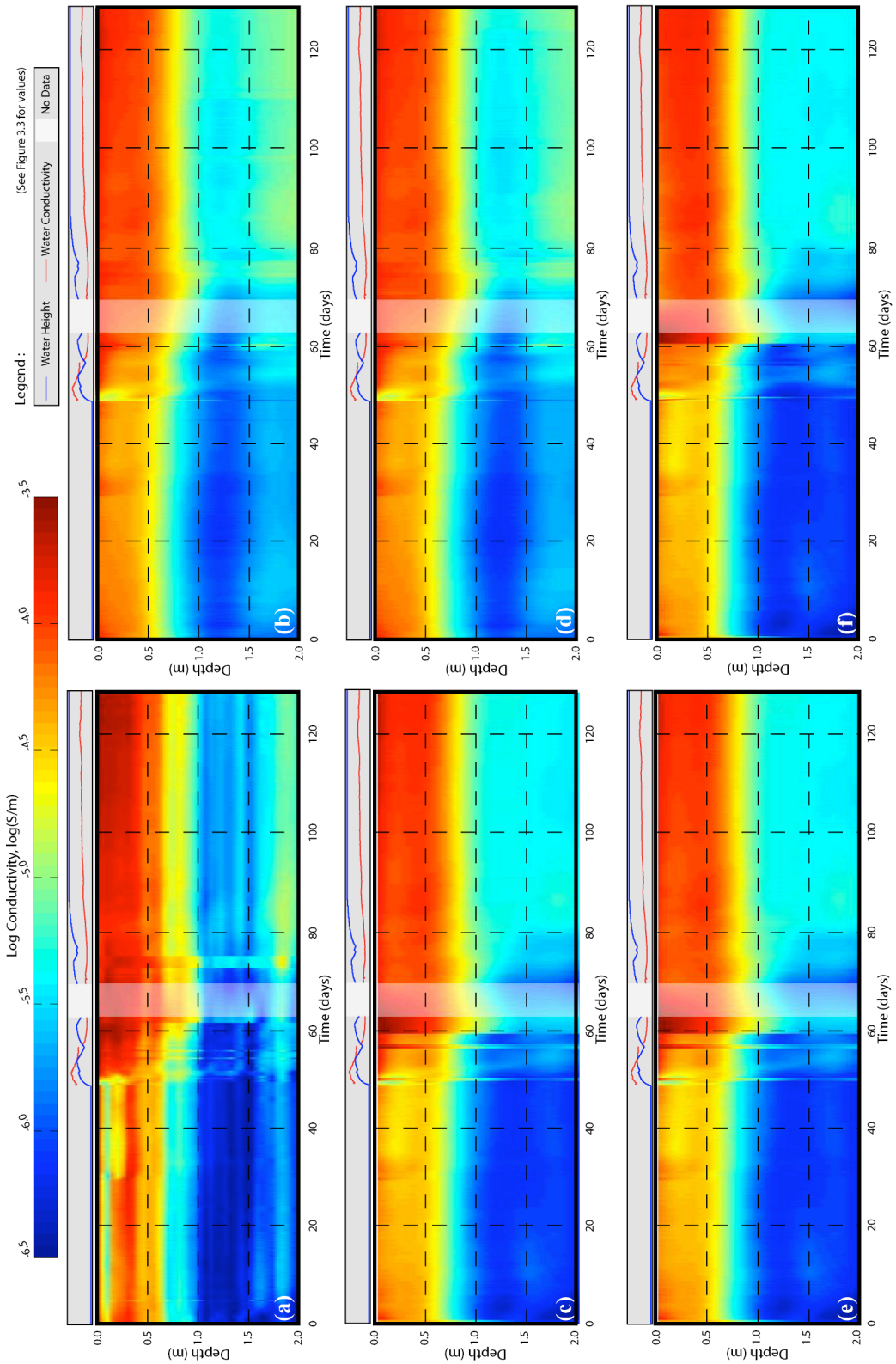

Figure 3-8: Probe 4 inversions shown in log conductivity; see Table 3.1 for descriptions.

3.6 Summary of the Inversions

The constraints placed on the inversion process and the starting model significantly affect the inversion results. It was found that constraining the EC of the water column, when this information was available, consistently reduced the inversion error the most of the six methods applied. Allowing for a conductive layer against the length of the probe increased inversion error for the majority of the experiment; however, using this method on Probe 3 produced the smoothest results in time, and had the lowest initial data misfit errors going into the inversion process. In all probes there were unexplained discontinuities in time that were likely numerical anomalies of the inversion process; inverting with respect to time and applying a smoothing constraint may address this problem.

The three probes had similar responses over time with increasing EC when the pond was filled with water. The depth of total saturation likely differed between locations and indicates spatial heterogeneity of infiltration rates and soil texture. Probe 2 shows differing signals with depth indicating spatial differences in the parameters EC is sensitive to; variability in water saturations is the likely cause.

3.7 Future Directions

In the sediment surrounding Probe 2, using Ref_N.nS.W, it was inferred that approximately the top 40cm of sediment are at 100% saturation (Figure 3.6). This inference is based on the majority of the EC response mimicking the fluid EC of the water column, not the water column height. Additionally, the conceptual model of the infiltration experiment suggests fully saturated conditions in the sediment when under 1 to 5m of water. However, by using Archie's law, it is possible to calculate the apparent saturation. Note that the quantitative link between water saturation and EC is still poorly understood. Archie's law (Eq. 1.9) requires that the bulk EC of the sediment be normalized by the fluid EC; this normalization can be approximated by using the EC of the water column. This assumption is valid if the fluid EC does not change upon entering the sediment and there is no lag time for the fluid to enter the sediment. Figure 3.9a shows the bulk EC normalized by the fluid EC, which yields the inverse of Archie's

formation factor, for the top 40cm from the time when the pumps are turned on. It is apparent that this formation factor varies with time; however, this parameter is theorized to be a constant for a given formation (Archie, 1942). This variability indicates temporal variability of porosity, saturation, the cementation exponent, and/or the saturation exponent. For the sake of example, let it be assumed that all variability is due to changes in saturation. Assuming the cementation exponent to be constant, and calculating it using the 10 highest EC values assuming these correspond to 100% saturation yields m=1.302. Using this value for the cementation exponent, a literature value for the saturation exponent (n = 2), and an assumed porosity value for unconsolidated sand (0.40), it is possible to obtain an apparent saturation map of this area (Figure 3.9b). However, this saturation map does not agree with the conceptual model of the top 40cm (i.e. we expect S_w = 1), and it is likely that other parameters are changing with time. In the top 10cm this model predicts that the water saturation is below 60%; this is unlikely and decreases in EC could be due to porosity reductions, variations in surface area, or increases in electrical tortuosity. Further analysis of this dataset is needed to link EC measurements to hydrogeologic parameters. The results from the numerical model will also be applied to these inversions to help analyze the data with respect to reductions in porosity and pore geometry. The rock-physics relations created by our numerical model are in the same range and could help glean information about changes in the cementation exponent and porosity.

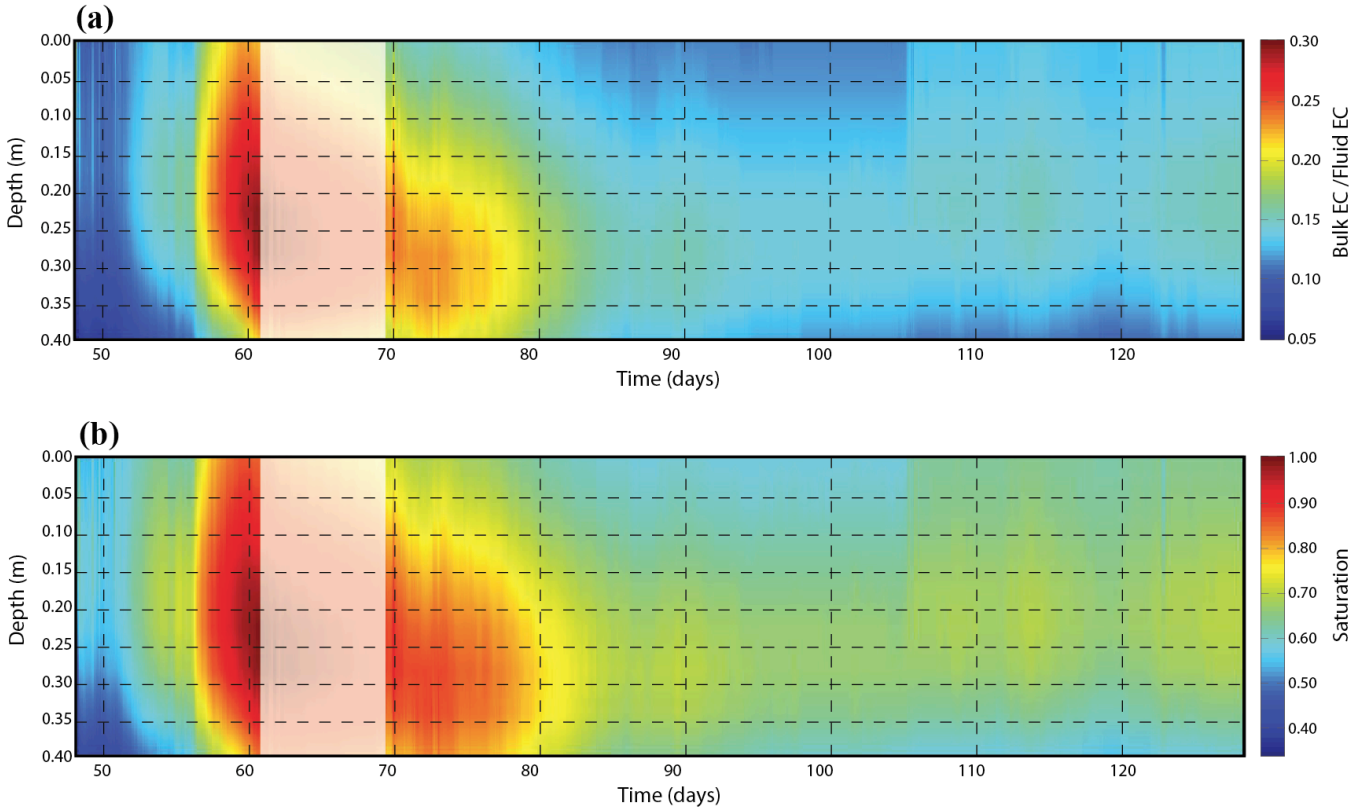

Figure 3-9: Top 40 cm of Probe two using inversion Ref_N.nS.W over the infiltration experiment; temporal variability in (a) Archie's formation factor and (b) saturation are apparent.

3.8 Contributions

The first steps of a methodology were created for the analysis of the data from the high-quality time-lapse EC probes. As well initial observations and a plan to move forward in the analysis of this data has been created. Multiple codes were written for this process especially visualization programs for sorting and viewing the large amount of data in an organized fashion (Table 3.2). The integration of large amounts of data was necessary to create inversion driver files that were easily understood and repeatable. Additionally, a graphical user interface was created that provided access to all inversion data; temporal changes in conductivity were viewable in a movie format (Figure 3.10). The inversion data must still be rigorously interpreted with respect to changes in porosity, saturation, and Archie exponents; this analysis will be significantly easier with efficient data processing tools.

Table 3.2: Titles and explanation of code developed in Matlab for the inversion process.

Code Title	Description
Inv_Surfer (Figure 3.10)	- Creation of a graphical user interface that allows users to flip through multiple inversion methods, time, and probes. - Program shows cylindrical cross section and line plots of conductivity at different distances - Plots are in either resistivity or conductivity
Water Height Calculation	- Integration of the universal water column height to specific probe elevations.
Grid Compiler	- Programs that create computational and inversion grids based on the water column height.
Parameter File Creation	- Data sorting and initial conductivity calculations of the probe data.
Driver Code	- Creation of driver files for inversions that include *a priori* information.
Cube_it	- Creation of data cubes with vertical, radial, and time dimensions
Visualization Code	- Visualization techniques using Matlab software for viewing data over time and at depth.

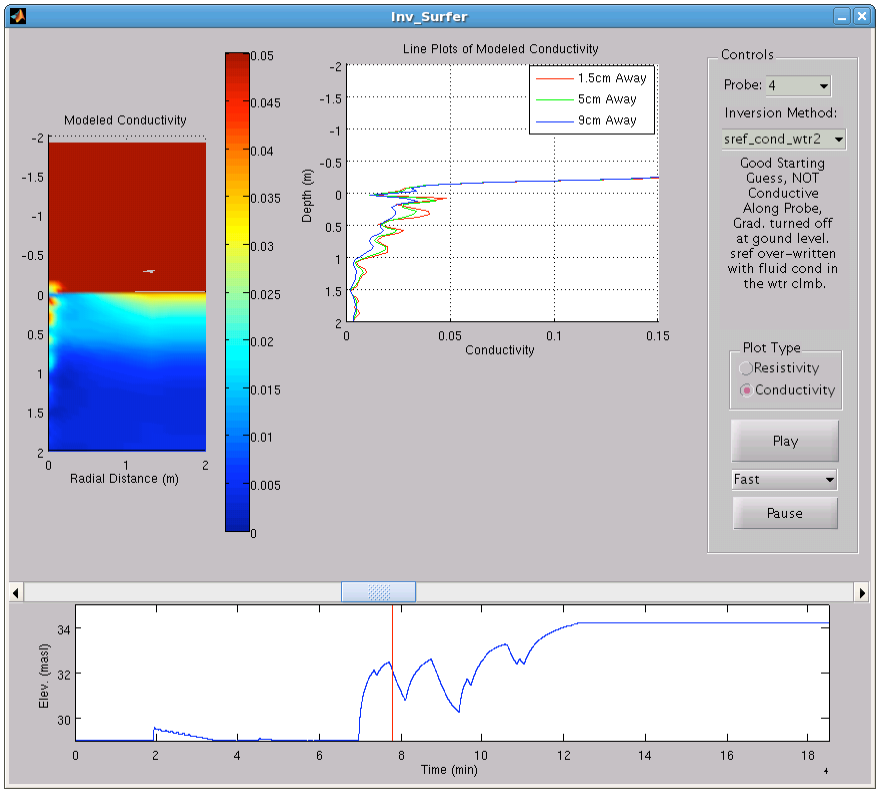

Figure 3-10: Screen capture of Inv_Surfer, which allows users to interface with multiple inversion methods and create movies of sediment changes through time.

Chapter Four: Summary and Conclusions

This project stems from ongoing geophysical research focused on optimizing the efficiency of an artificial recharge pond near Santa Cruz, California. The practicality of subsurface water storage is being investigated in an area where overuse of aquifers has led to water table drawdown and saltwater intrusion. The goal of the artificial recharge pond is to provide local water users with an alternative water source such that the demand on the main aquifer, which is threatened, is reduced.

A seasonal groundwater recharge pond was created, and in the winter of 2008, observed infiltration rates at the recharge pond were well below expected values, and consequently the recharge pond yielded a poor return the following summer. The winter of 2009 is the second year that multiple 1-D EC probes were installed to monitor the change in infiltration as a function of time. Each probe is equipped with 25 electrodes that measure changes in bulk EC beneath the pond every 18 minutes during infiltration. A major operational issue at this site is the fact that infiltration rates slow drastically with time. This slowing limits the volume of water that can be stored during the season, and hence, the overall productivity of the system. Key to understanding this issue is assessing the timing, mechanism, and spatial variability of these changes in infiltration. Electrical conductivity is a geophysical property that is very sensitive to water content and quality as well as pore geometry.

Of particular interest for this thesis, was the use of EC to monitor the changes in soil properties over the duration of the infiltration experiment. The overall goal of the project is to use EC to calibrate a hydrologic model of the site that can be incorporated into a better management plan of the recharge pond. However, in order to do this, the EC probe data needs to be inverted to yield comprehensive EC estimates, these EC values then need to be interpreted in terms of changes in porosity and saturation. This interpretation has many challenges, as the measured EC is not only a function of soil matrix, but also fluid conductivity and saturation. Thus, before EC data can be interpreted, a rigorous conceptual model of the hydrogeologic parameters at play, and how these parameters change with time, must be well understood. This thesis focuses on (1) the conceptual model of hydrogeologic processes effecting EC at the pore scale; and

(2) investigation of the inversion methodology necessary to interpret the field data from the EC probes.

Developing the pore scale conceptual model was the driving force behind the numerical modeling focused on in Chapter 2. Time-lapse reductions in porosity and changes in the pore space arrangements were created through two algorithms; Add: a simulation of addition of fine-grained material to the matrix; and Grow: a simulation of biological growth and the creation of biofilms. These two mechanisms allowed an in-depth study of EC with respect to porosity, specific surface area, and electrical tortuosity. Significant amounts of code were created that can be reused and developed to implement biofilm conduction studies, and possible hydraulic conductivity and tortuosity simulations. The utility of Archie's law was also explored at the pore scale including ranges and expected temporal variability with changes in porosity. Multiple rock physics relationships were created that link Archie's formation factor to changes in porosity. Variability in Archie's cementation exponent was also explored, and very different responses were found between the two clogging mechanisms. The conceptual model created about temporal variability in unconsolidated porous media is key to analyzing field data and identifying possible limitations of empirical equations.

Inversion of the field data was the primary focus of Chapter 3. The inversion methodology, and inclusion of *a priori* information such as smoothing, water column height, and discontinuities was crucial to the final time-lapse inversion image. It was found that there were anomalous discontinuities in the time axis of this inversion image; a comprehensive inversion process that allowed for smoothing constraints over time may solve these problems. The interpretation of the conductivity profiles will incorporate the knowledge gained by the numerical model. The range of porosity, formation factor, and the cementation exponent calculated in the numerical model match the field data. It is seen that the formation factor decreases with time in the pond, this trend is mimicked by the infiltration rate; porosity reductions similar to those simulated in the numerical model are likely. In future work I will integrate my numerical model with the field data to interpret the EC probe results in the context of pore clogging, to help gain insight in the top two meters of Harkins recharge pond. Interpretation of the final EC images will also

likely involve incorporating data on temperature and water chemistry collected from the probes, to try and infer the mechanisms behind the decreasing infiltration rate over time. Knowledge of the mechanism behind the decreased infiltration rate is crucial to creating a mitigation scheme that can increase infiltration in the artificial recharge pond, and consequently decrease the demand on the groundwater resources of the region.

References

Archie, G. E. (1942). The electrical resistivity log as an aid in determining some reservoir characteristics. *Transactions of the American Institute of Mechanical Engineers, 146*, 54-61.

Atekwana, E. A., Sauck, W. A., & Werkema, D. D. (2000). Investigations of geoelectrical signatures at a hydrocarbon contaminated site. *Journal of Applied Geophysics, 44*(2-3), 167-180.

Atekwana, E. A., Werkema, D. D., & Atekwana, E. A., (2006), Biogeophysics : the effects of microbial processes on geophysica properties of the shallow surface. *Applied Hydrogeophysics*. 161-193

Azar, J. H., Javaherian, A., Pishvaie, M. R., & Nabi-Bidhendi, M. (2008). An approach to defining tortuosity and cementation factor in carbonate reservoir rocks. *Journal of Petroleum Science and Engineering, 60*(2), 125-131.

Benson, A. K., Payne, K. L., & Stubben, M. A. (1997). Mapping groundwater contamination using dc resistivity and VLF geophysical methods--A case study. *Geophysics, 62*(1), 80-86.

Bopp, S., Weiß, H., & Schirmer, K. (2005). Time-integrated monitoring of polycyclic aromatic hydrocarbons (PAHs) in groundwater using the ceramic dosimeter passive sampling device. *Journal of Chromatography A, 1072*(1), 137-147.

Boving, T. B., & Grathwohl, P. (2001). Tracer diffusion coefficients in sedimentary rocks: Correlation to porosity and hydraulic conductivity. *Journal of Contaminant Hydrology, 53*(1-2), 85-100.

Carman, P. C. (1950). Diffusion and flow of gases and vapours through micropores. I. slip flow and molecular streaming. *Proceedings of the Royal Society of London.Series A, Mathematical and Physical Sciences, 203*(1072), 55-74.

Deiana, R., Cassiani, G., Villa, A., Bagliani, A., & Bruno, V. (2008). Calibration of a vadose zone model using water injection monitored by GPR and electrical resistance tomography. *Vadose Zone Journal, 7*(1), 215-226.

French, H., & Binley, A. (2004). Snowmelt infiltration: Monitoring temporal and spatial variability using time-lapse electrical resistivity. *Journal of Hydrology, 297*(1-4), 174-186.

GanerÃ¸d, G., RÃ¸nning, J., Dalsegg, E., Elvebakk, H., HolmÃ¸y, K., Nilsen, B., *et al.*, (2006). Comparison of geophysical methods for sub-surface mapping of faults and fracture zones in a section of the viggja road tunnel, Norway. *Bulletin of Engineering Geology and the Environment, 65*(3), 231-243.

Garambois, S., Sénéchal, P., & Perroud, H. (2002). On the use of combined geophysical methods to assess water content and water conductivity of near-surface formations. *Journal of Hydrology, 259*(1-4), 32-48.

Glover, P. (2009). What is the cementation exponent? A new interpretation. *The Leading Edge, 28*(1), 82-85.

Haines, S. S., Pidlisecy, A., & Knight, R. (2009). Hydrogeologic structure underlying a recharge pond delineated with shear-wave seismic reflection and cone penetrometer data. *Near Surface Geophysics, 7*(5-6), 329-339.

Harinarayana, T. (1999). Combination of EM and DC measurements for upper crustal studies. *Surveys in Geophysics, 20*(3), 257-278.

Hayashi, M. (2004). Temperature-electrical conductivity relation of water for environmental monitoring and geophysical data inversion. *Environmental Monitoring and Assessment, 96*(1), 119-128.

Herrick, D. C., & Kennedy, W. D. (1994). Electrical efficiency---A pore geometric theory for interpreting the electrical properties of reservoir rocks. *Geophysics, 59*(6), 918-927.

Hirono, T., Nakashima, S., & Spiers, C. J. (2008). Measurements of ionic diffusivity in various rock samples: Low diffusivity through nanoscale pores. *International Journal of Rock Mechanics and Mining Sciences, 45*(3), 450-459.

Hu, Q., & Wang, J. S. Y. (2003). Aqueous-phase diffusion in unsaturated geologic media: A review. *Critical Reviews in Environmental Science and Technology, 33*(3), 275-297.

Jayawickreme, D. H., Van Dam, R. L., & Hyndman, D. W. (2008). Subsurface imaging of vegetation, climate, and root-zone moisture interactions. *Geophysical Research Letters, 35*

Jodrey, W. S., & Tory, E. M. (1979). Simulation of random packing of spheres. *Simulation, 32*(1), 1-12.

Lovell, M. A., Jackson, P. D., Harvey, P. K., Williams, C. G., Flint, R. C., Williamson, G., *et al.*, (1998). Electrical resistivity measurements on unconsolidated core. *The Society of Core Analysts, 35*, 1-12.

Martin, H., Patterson, B. M., Davis, G. B., & Grathwohl, P. (2003). Field trial of contaminant groundwater monitoring: Comparing time-integrating ceramic dosimeters and conventional water sampling. *Environmental Science & Technology, 37*(7), 1360-1364.

Mendelson, K. S., & Cohen, M. H. (1982). The effect of grain anisotropy on the electrical properties of sedimentary rocks. *Geophysics, 47*(2), 257-263.

Worthington, P.F. (1993). The uses and abuses of the archie equations, 1: The formation factor-porosity relationship. *Journal of Applied Geophysics, 30*, 215-228.

Pidlisecky, A., Haber, E., & Knight, R. (2007). RESINVM3D: A 3D resistivity inversion package. *Society of Exploration Geophysicists, 72*(2), H1-H10.

Racz, A. J., Fisher, A. T., Schmidt, C. M., Lockwood, B. S., & Los Huertos, M. (2009). Spatial and temporal variations in seepage during managed aquifer recharge [Abstract]. *Eos Trans. AGU, 90*(52)

Rein, A., Hoffmann, R., & Dietrich, P. (2004). Influence of natural time-dependent variations of electrical conductivity on DC resistivity measurements. *Journal of Hydrology, 285*(1-4), 215-232.

Roberts, J. N., & Schwartz, L. M. (1985). Grain consolidation and electrical conductivity in porous media. *Phys.Rev.B, 31*(9), 5990-5997.

Sen, P. N., Scala, C., & Cohen, M. H. (1981). A self-similar model for sedimentary rocks with application to the dielectric constant of fused glass beads. *Geophysics, 46*(5), 781-795.

Sénéchal, P., Perroud, H., Kedziorek, M. A. M., Bourg, A. C. M., & Gloaguen, E. (2005). Non destructive geophysical monitoring of water content and fluid conductivity anomalies in the near surface at the border of an agricultural field. *Subsurface Sensing Technologies and Applications, 6*(2), 167-192.

Shackelford, C. D. (1991). Laboratory diffusion testing for waste disposal — A review. *Journal of Contaminant Hydrology, 7*(3), 177-217.

Singha, K., & Gorelick, S. M. (2006). Effects of spatially variable resolution on field-scale estimates of tracer concentration from electrical inversions using Archie's law. *Society of Exploration Geophysicists, 71*(3), G83-G91.

Singha, K., Pidlisecky, A., Day-Lewis, F., & Gooseff, M. N. (2008). Electrical characterization of non-fickian transport in groundwater and hyporheic systems. *Water Resources Research, 44*, W00D07.

Spearing, M., & Matthews, G. P. (1991). Modelling characteristic properties of sandstones. *Transport in Porous Media, 6*(1), 71-90.

Suman, R., & Ruth, D. (1993). Formation factor and tortuosity of homogeneous porous media. *Transport in Porous Media, 12*(2), 185-206.

Telford, W. M., Geldart, L. P., & Sheriff, R. E. (1990). *Applied Geophysics* (Second ed.).

Weisstein, Eric W. "Spherical Cap." From MathWorld--A Wolfram Web Resource. http://mathworld.wolfram.com/SphericalCap.html

Werkema, D. D., Atekwana, E. A., Endres, A. L., Sauck, W. A., & Cassidy, D. P. (2003). Investigating the geoelectrical response of hydrocarbon contamination undergoing biodegradation. *Geophysical Research Letters, 30*(12), 1647.

Wyllie, M. R. J., & Spangler, M. B. (1952). Application of electrical resistivity measurements to problem of fluid flow in porous media. *Bulletin of the Amer. Ass. Of Pet. Geologists, 36*, 359-403.